Catena 256 (2025) 109123

Contents lists available at ScienceDirect

Catena

journal homepage: www.elsevier.com/locate/catena

Climate dynamics during the last 3000 years forced environmental and sedimentation changes in southern Spain: The Laguna Grande de Archidona record

Gonzalo Jiménez-Moreno [a,*], Antonio García-Alix [a,b], Fernando Gázquez [c,d], Aurora Castillo-Baquera [a,c], Lucía Martegani [c,d], Miguel Rodríguez-Rodríguez [e], Marta Rodrigo-Gámiz [a], Francisco J. Jiménez-Espejo [b]

[a] Departamento de Estratigrafía y Paleontología, Universidad de Granada, Spain
[b] Instituto Andaluz de Ciencias de la Tierra (IACT), CSIC-UGR, Armilla, Spain
[c] Department of Biology and Geology. University of Almería, Almería, Spain
[d] Andalusian Centre for Global Change – Hermelindo Castro University of Almería, Spain
[e] Physical, Chemical and Natural Systems, Pablo de Olavide University, Seville, Spain

ARTICLE INFO

Dataset link: Geochemistry data LGA (Original data)

Keywords:
Vegetation
Sedimentation
Climate
Human impact
Late Holocene
Western Mediterranean

ABSTRACT

A geochemical, mineralogical, and sedimentological analysis of the sedimentary record from Laguna Grande de Archidona (LGA), a lake in southern Spain, produced a high-resolution climate and human activity record for the southwestern Mediterranean over the past three millennia. Lake level changes, organic matter, and gypsum intervals were primarily driven by precipitation and hydrological shifts. From 3300 to 2600 cal yr BP, dry conditions prevailed, particularly from 3050 to 2600 cal yr BP, coinciding with a regional drought tied to a positive North Atlantic Oscillation (NAO). The wettest period, from 2600 to 1400 cal yr BP during the Iberian Roman Humid Period (IRHP), was marked by increased groundwater and lake stratification due to negative NAO, which generated the precipitation of gypsum and manganese oxides. However, this relatively wetter period was interrupted by two arid events between 2300–2200 and 2150–2050 cal yr BP. A dry phase spanned the Dark Ages through the Medieval Climate Anomaly (MCA; 1400–700 cal yr BP), while the Little Ice Age (LIA) showed varied but generally wetter conditions, followed by an arid period from ~1600–1850 CE. The Industrial Epoch (1850–1957 CE) also saw dryness, with late 20th-century changes attributed to modern climate impacts and irrigation practices.

1. Introduction

Anthropogenic activities since the second half of the 19th century have caused global temperatures to rise, reaching unprecedent levels of the last millennia (IPCC, 2022). The analysis of the last 112 years of instrumental climatological data from the southern Iberian Peninsula also shows an increasing long-term trend in drought conditions that is largely due to the evapotranspiration enhancement as result of the global temperature rise (Páscoa et al., 2017). Previous studies have also documented a higher frequency of extreme heat waves in recent years, especially during the summer (Sousa et al., 2019), which is intensifying the effects of drought. This is having a tremendous impact on water, ecological and social resources, apart from serious economic implications in this region, as agricultural and livestock production is also being significantly reduced (Hervás-Gámez and Delgado-Ramos, 2019; Peña-Gallardo et al., 2019).

Generating paleoclimate reconstructions is essential for situating post-industrial warming and drought increase into the context of natural climate variability (PAGES2k Consortium, 2017). In addition, understanding the long-term relationship between environmental change with climate and human perturbations in the Mediterranean basin can help assessing the ecosystem response and resilience to the enhancement of those perturbations (MedECC, 2020). However, obtaining such high-resolution sediment records of the last millennia in the southern Iberian Peninsula is challenging due to both the scarcity of permanent lakes in this region and also to the increased aridity recorded during the Late

* Corresponding author.
E-mail address: gonzaloj@ugr.es (G. Jiménez-Moreno).

https://doi.org/10.1016/j.catena.2025.109123
Received 30 October 2024; Received in revised form 10 April 2025; Accepted 1 May 2025
Available online 6 May 2025

Holocene. Such aridification has led to the transformation of many lakes from permanent to seasonal (López-Avilés et al., 2022; García-Alix et al., 2022). Finally, human disturbances in many wetlands may have altered sedimentary records in some of these lakes (Jiménez-Bonilla et al., 2023; Gázquez et al., 2023).

Different climate/environmental indicators can be applied in continental sedimentary sequences. Changes in the physical (i.e., lithology, color, magnetic susceptibility) and chemical (i.e., mineralogy, elemental composition) characteristics of lake deposits provide information about past environmental and climate conditions. For example, magnetic susceptibility (MS) is commonly used in lacustrine deposits as a proxy for detrital input of magnetic minerals, generally associated with enhancement of erosive and/or fluvial transport processes (e.g., Camuera et al., 2018). The occurrence of evaporites, such as gypsum, in lacustrine sediments has traditionally been interpreted as an indicator of dry periods (Martín-Puertas et al., 2010; Evans et al., 2018; Gázquez et al., 2023) or enhanced evaporation/precipitation balance (García-Alix et al., 2022). Lastly, the organic elemental and isotopic composition of bulk sediment (i.e., TOC or C/N atomic ratios) has been used to interpret the main features of the organic fraction in lacustrine sedimentary records, such as lake productivity or the source of the organic matter (Meyers, 1994). Elemental composition, measured at high-resolution by X-ray fluorescence scanner (XRF core scanning) is a useful non-destructive tool that facilitates a comprehensive understanding

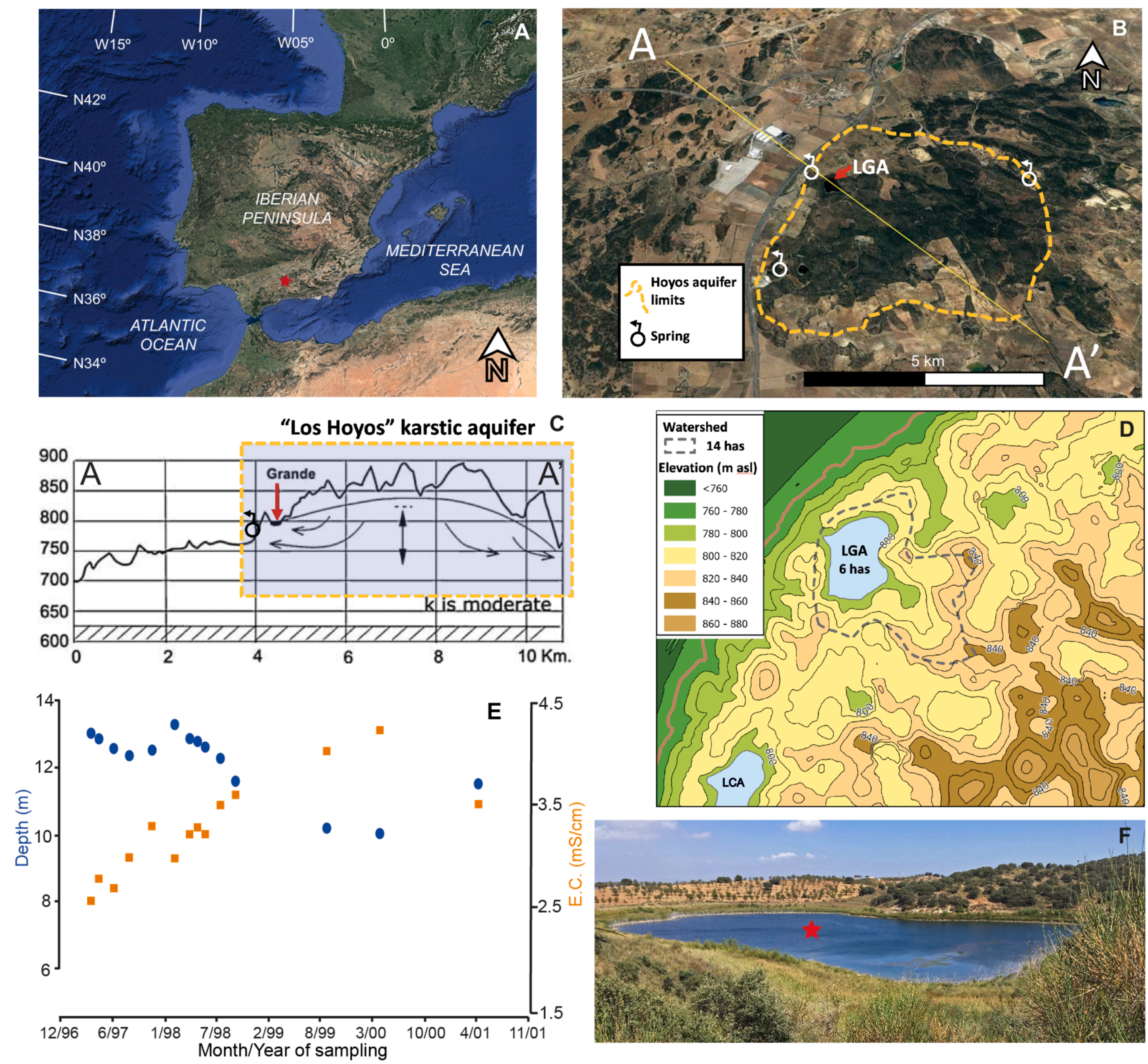

Fig. 1. Location and hydrogeologic setting of the study site Laguna Grande de Archidona (LGA). (A) Location of LGA in the southern Iberian Peninsula. (B) Topography and watershed limits of LGA. Aerial photo showing the approximate limits of Los Hoyos karstic aquifer and position of LGA in relation to it. Laguna Chica (LCA) is also shown. (C) Cross section of the aquifer. Note that the phreatic level intersects LGA in the western border of the aquifer. Arrows indicate the direction of the groundwater flow, to LGA and to Molino spring (also shown). Arrows indicate main groundwater flow directions. Slope (0 % = flat, 100 % = 1:1). (D) Topographic map showing LGA and its watershed. (E) Diagram showing measurements of lake level (depth in meters) and salinity (in miliSiemens/cm) between 1996 and 2001. Note that salinity increases during lowering of lake level and vice versa. (F) Photograph of LGA and sediment core location (red star). Note the almond and olive crops on the background.

of the chemical elemental composition of sediment cores. This analytical technique has proved invaluable in paleoclimatic studies (e.g., Bertrand et al., 2024). The efficacy of XRF-scan depends on a thorough understanding of the numerous factors potentially influencing the composition of both major and trace elements within sediments (e.g., Jiménez-Espejo et al., 2014; Vizcaino et al., 2022).

In this regard, the multiproxy high-resolution study of the sedimentary record of Laguna Grande de Archidona (LGA) combining the methods mentioned above, provides us with high-quality and detailed information on sedimentation and lake dynamics over the past ~ 3 millennia due to climate change and anthropogenic impact in southern Spain. The comparison of the LGA record with other paleoclimatic records from southern Iberia and the western Mediterranean further permit to obtain information on potential climatic and anthropogenic factors causing paleoenvironmental changes in the study area.

2. Study site

2.1. Geographic setting

LGA (37°06′28.30′'N; 4°18′14.88′'W; 794 m a.s.l.) forms part of the Archidona Lakes Nature Reserve, a protected wetland located near the towns of Salinas and Archidona, in the province of Málaga, southern Spain (Fig. 1). The Archidona lakes are located in endorheic basins, bear brackish to saline waters, and are home to numerous species of birds. The nature reserve occupies an area of ~ 0.06 km^2 and is surrounded by a peripheral zone of 1.87 km^2, adding up to a total of 1.93 km^2 of protected area. The Archidona lakes consist of two water bodies, LGA, to the north, and Laguna Chica (LCA), to the south (Fig. 1C and 1D). The average flooded surface of LGA is 0.06 km^2 and its watershed is relatively small (0.14 km^2) (Fig. 1D). The average slope of the watershed is 17.4 % (calculated using this formula: elevation change/horizontal distance*100). LGA maximum depth is 13.4 m, being one of the deepest natural lake systems in southern Spain.

Climate in the area is continental Mediterranean, with dry and hot summers and cool and wet winters. The mean annual temperature in the nearby Archidona meteorological station (https://www.juntadeandalucia.es/agriculturaypesca) is 15.9 °C. The highest temperatures are recorded during the summer months, with mean temperatures in July and August, of 26.2 and 25.7 °C, respectively. The lowest mean monthly temperatures occur in winter, reaching the minimum in January, with 7.4 °C. The North Atlantic Oscillation (NAO), a large-scale atmospheric pressure pattern between the Azores High (subtropical high pressure) and the Icelandic Low (subpolar low pressure), plays a key role in the precipitation variability in southern Spain, influencing both seasonal and interannual rainfall patterns (Hurrell et al., 2013). During NAO + years (strong Azores High and deep Icelandic Low), the westerlies are strengthened pushing storms northward, leading to less precipitation and increased drought risk in southern Spain. During NAO- years (weak Azores High and weak Icelandic Low), the weaking of the Azores High allows storm tracks to shift southward, bringing more Atlantic moisture and precipitation to southern Spain, especially during winter (Hurrell et al., 2013). Most of the precipitation in the area occurs from October to May (winter *sensu lato*), with a maximum in the month of December due to the action of the Atlantic humid westerlies. In spring, the humid westerlies and higher temperatures produce rainstorms. Mean annual precipitation from 2017 to 2023 was 418 mm/year, which contrasts with the average precipitation during the last quarter of the 20th century of 614 mm/year. This reduction in the available water resources in the area is notably affecting the soil water budget. In some exceptionally dry years (e.g., 2015, 2017) surplus from the soil water budget (i.e., runoff + groundwater recharge to the aquifers) for a water holding capacity of 100 mm was negligible (no surplus at all). On the other hand, average evaporation is much higher (1500 mm during the period 2015–2021 vs. 1300 mm during the period 1974–1996). This situation, together with the intensive olive crop irrigation since the 90′s (Hidalgo-Moya et al., 2007), is significantly stressing the aquatic ecosystems in southern Spain since the last decade. As an example, the LGA level has gradually decreased from 13.4 to 7 m deep in the period 2013–2023 (Nature Reserve unpublished data).

Natural tree vegetation in the LGA area is characterized by the predominance of mesomediterranean vegetation belt (between 700–1300 m; Rivas-Martínez, 1987) with evergreen oaks (*Quercus rotundifolia*), wild olive trees (*Olea europaea* var. *sylvestris*) and fewer deciduous oaks (*Q. faginea*). *Crataegus*, *Retama*, *Rosa*, *Ulex*, *Genista, Pistacia lentiscus,* and *Phlomis* are the characteristic shrubs in the area. Herbs are dominated by several species of Poaceae, Asteraceae, Lamiaceae and Amaranthaceae. Anthropogenic activities in the study region are mostly characterized by *Prunus dulcis* (almond) and *Olea* (olive) crops and cereal and sunflower seed cultivation. Almond and olive crops occur immediately north and southwest of the lake, respectively. LGA is immediately surrounded by a dense *Juncus,* Cyperaceae (mostly *Scirpus*) and *Tamarix* belt that makes access to the shore difficult. LGA is colonized by different communities of aquatic submerged macrophytes including *Potamogeton*, *Myriophyllum* and *Chara* (Caracterización Ambiental de Humedales en Andalucía, 2005).

2.2. Geological setting

LGA is located in the Subbetic Unit of the Betic Cordillera where the geology is characterized by the presence of rocks of Triassic age at the base of the stratigraphic sequence (Vera, 2004). LGA occurs in one of those Triassic outcrops characterized by a melange of clays, marls and evaporitic rocks, such as gypsum, with karstic geomorphology. These rocks occur in the area due to diapiric processes (e.g., Calaforra and Pulido-Bosch, 1999). The formation of brackish and saline lakes there are due to several geological mechanisms that generated closed depressions forming ephemeral to permanent shallow lakes. In some cases, including LGA, lakes formed because of exo- and *endo*-karstic processes (e.g., dissolution of gypsum and halite). LGA formed within a large diapiric dome locally named “Los Hoyos” (Holes in English). The main geomorphological characteristic of “Los Hoyos” area (Fig. 1) is the existence of numerous bowl-shaped dolines. A significant number of such dolines occur in the central part of the dome, where gypsum materials constitute the nucleus of the structure (Carrasco et al. 2004; Fig. 1). Other dolines, including LGA, developed at lower elevation at the edge of the central sector, and they are flooded due to the intersection of the bottom of the doline with the regional phreatic level of the aquifer (Rodríguez-Rodríguez and Benavente, 2008). LGA is located near a contact between the karst aquifer and Triassic marls that constitute the impermeable sealing of the aquifer (Fig. 1C).

2.3. Hydrogeological functioning of LGA

“Los Hoyos” dome is an unconfined karstic aquifer with a recharge area of several square kilometers and a moderate permeability due to the predominance of clays, marls and gypsum rocks (Carrasco et al., 2004). Recharge takes place mainly via rainwater infiltration. The groundwater discharge is radial towards the edges of the dome (Fig. 1C). LGA is in the western sector of the dome where groundwater discharges to the lake and to nearby springs. The LGA system receives groundwater discharge enriched in solutes from the aquifer when the aquifer level rises, only after relatively wet periods. However, during dry periods, evapotranspiration is the sole factor contributing to the lowering of the lake level. This suggests that the lake is supplied by the aquifer during times of high groundwater levels but does not lose water to the aquifer, indicating that it is not a recharge lake (Jimenez-Bonilla et al., in preparation). This hydrological functioning is in accordance with the water budget results in this lake (Rodríguez-Rodríguez and Benavente, 2008). Water inputs are regional groundwater discharge from the karstic aquifer and surface and subsurface run-off from the watershed (Fig. 1C and 1D). Water outputs are mainly by evaporation and, only occasionally, by overflow, when the lake reaches more than 13.4 m of water column (Gil-Márzquez et al., 2016). This only occurs during exceptionally humid periods. LGA can be classified as a warm monomictic lake, with a mixing period lasting from September to February. In summer, a thermocline develops at a depth of 6 m. Electrical conductivity in the water column of LGA remained virtually constant throughout the year (Rodriguez-Rodriguez et al., 2011; Gil-Márquez et al., 2016). Salinity in the lake water increases seasonally during summer and especially during dry phases, when the lake level drops (Rodríguez-Rodríguez, 2002; Fig. 1E). The electrical conductivity of the water gradually increased from 4.2 to up to 7.6 mS/cm between 2020 and 2024, because of a ~ 6.5 m lake level drop (unpublished results). The karstification that affects the LGA area mainly occurred in Triassic gypsum materials, and previous water composition analyses in LGA classify them as calcium sulfated (Rodríguez-Rodríguez et al., 2001).

3. Materials and methods

The 276 cm-long LGA sedimentary record, a composite record from two adjacent sediment cores, LGA-19–03 short core and LGA-19–04 long core, was recovered from the depocenter of the LGA basin from a floating platform anchored to shore in September 2019 using a universal corer with a plexiglass tube (Aquatic Research, Inc.) and a Livingstone square-rod piston corer (Fig. 2). Maximum lake depth when coring was 8.9 m.

The cores were transported to the University of Granada (UGR),

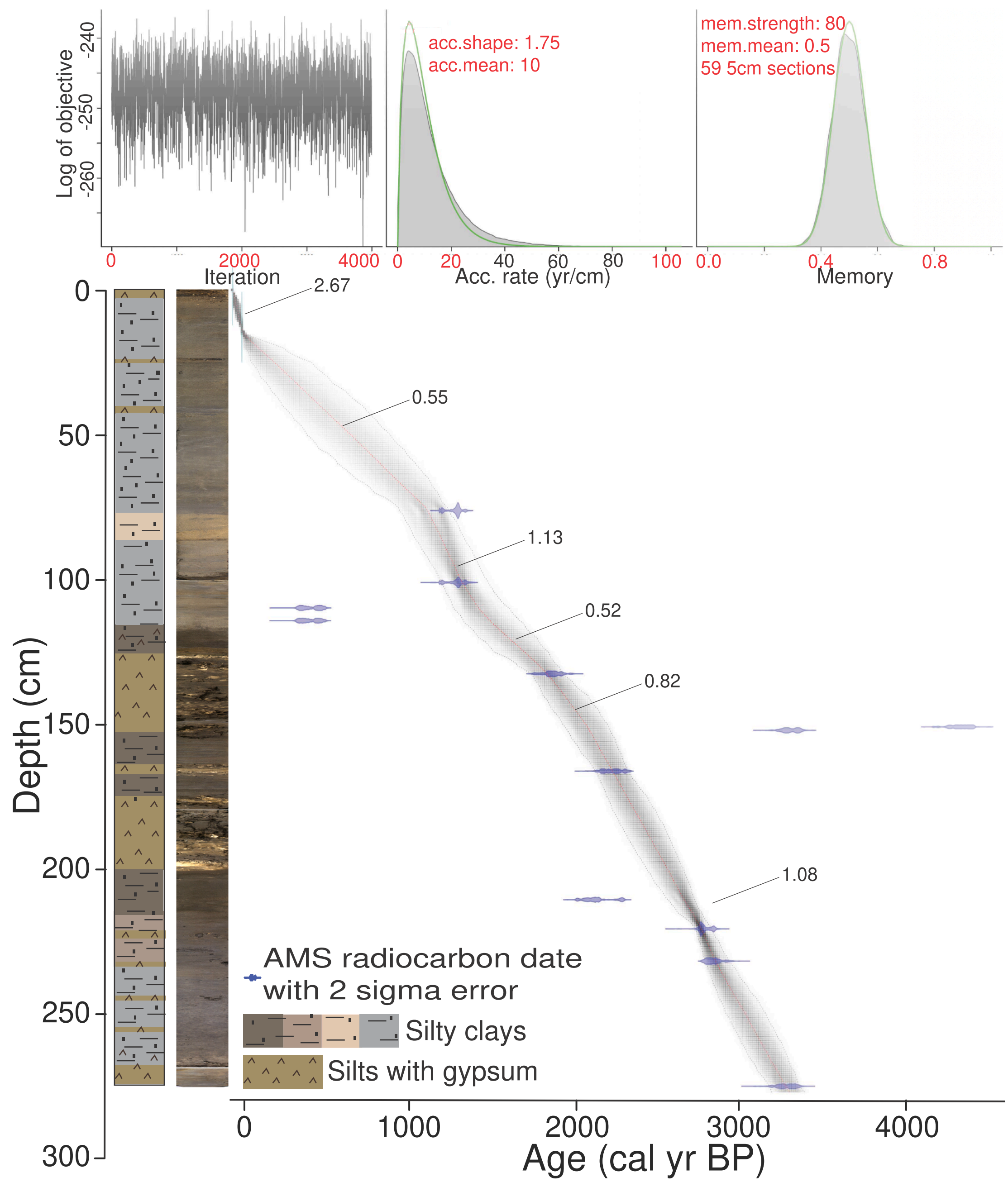

Fig. 2. LGA sedimentary record and Bayesian age model (95% confidence interval and red median line) with estimated sedimentary rates in mm/yr. The calibrated ^{14}C dates and their associated uncertainties are depicted in blue. The accumulation rate plot illustrates both the prior and posterior distribution of accumulation rates, with green and grey lines respectively. Similarly, the memory plot displays the prior and posterior distribution of model memory, again delineated by green and grey lines. The log-posterior time-series demonstrates a consistent and stable model performance.

stored in a refrigerated room at 4 °C and eventually were split and imaged in the laboratory at UGR and Centro de Instrumentación Científica (CIC, UGR), respectively. The lithology was described in the laboratory and magnetic susceptibility (MS), a measure of the tendency of sediment to carry a magnetic charge (Snowball and Sandgren, 2001), was measured continuously from the surface of the two cores every 0.5 cm using a Bartington MS2E meter in SI units (Fig. 2). MS was used for correlation of the short LGA-19–03 and the long LGA-19–04 cores and construction of the composite LGA-19 record, overlapping at 2.5 cm depth.

A $^{239+240}$Pu activity profile of 16 bulk sediment samples of the topmost ~ 20 cm and twelve Accelerator Mass Spectometry (AMS) radiocarbon dates, obtained from both plant remains and bulk organic samples, were used to constrain the age of the LGA-19 record (Table 1; Fig. 2). The Pu profile was analyzed at the Chemistry Department at Northern Arizona University (USA). The chemical procedures were adapted from those reported in Ketterer et al. (2004).

In the case of the AMS ^{14}C dates of bulk organic samples, a pretreatment with HCl 1 N and HF 1 N was applied to remove the carbonate and silicate content and concentrate the organic remains. Radiocarbon dates were calibrated into calendar years using the IntCal20.14c curve (Reimer et al., 2020). Finally, an age-depth model was established using the Bayesian R-based package "Rbacon" (version 3.2 – November 2023, Blaauw and Christen, 2011). The obtained results of the convergence test and the stable log-posterior time-series suggest a reliable age-depth model and good fitting. The selected parameters for the age-depth model are included in Fig. 2.

The analysis of the organic elemental composition in the LGA-19 record was crucial for deciphering key aspects of the organic fraction within the bulk sediment (Fig. 3). In this process, a total of 247 samples, each obtained at approximately 1 cm intervals, underwent freeze-drying and overnight decarbonation through acid digestion using 1 N HCl. Subsequently, the samples were rinsed and centrifuged with Milli-Q water until reaching a neutral pH, followed by another round of freeze-drying. The elemental composition (CN) of the decarbonated fraction was determined using an Elemental UNICUBE elemental analyzer at the Department of Stratigraphy and Paleontology (UGR). The disparity in weight between the bulk and decarbonated samples allowed for the determination of the carbonate fraction's percentage within each sample. The overall C and N content was then recalculated based on the original bulk sediment weight. Atomic C/N ratios were derived from the total organic carbon (%TOC) and total nitrogen (%TN) content. Additionally, carbon (δ^{13}C) and nitrogen (δ^{15}N) isotopes were analyzed in an aliquot of these samples by means of a Thermo DeltaV advantage IRMS with a coupled Thermo EA IsoLink elemental analyser at the CIC-UGR. Certified organic analytical standards (Elemental Microanalysis Ltd) peat 133,519 (δ^{13}C = -28.174 ± 0.04 ‰ V-PDB and δ^{15}N=+4.768 ± 0.11 ‰ AIR), wheat 354,738 (δ^{13}C = -27.21 ± 0.13 ‰ V-PDB and δ^{15}N=+2.73 ± 0.17 ‰ AIR) and shorgum 257,737 (δ^{13}C = -13.78 ± 0.17 ‰ V-PDB and δ^{15}N=+1.58 ± 0.15 ‰ AIR) were used as well as the internal standard EBD23 (δ^{13}C = –22.49 ± 0.12 ‰ V-PDB and δ^{15}N=+9.94 ± 0.14 ‰ AIR). A principal component analysis (PCA) of the C/N and isotopic (δ^{13}C and δ^{15}N) data was carried out using the Past 4.05 program (Hammer et al., 2001) to determine affinities between the different organic geochemical analyses (Fig. 3). PCA is a statistical technique employed to identify components that capture the maximum variance within multivariate data, as described by Hammer et al. (2001). These resultant components are linear combinations of the original variables. PCA is a valuable tool for data summarization, enabling the representation of complex information in a reduced form, such as distilling it down to just two variables (the first two components), facilitating easy graphical comparisons.

X-ray diffraction (XRD) analysis of sediment samples facilitated the identification of the principal mineral phases (Fig. 4). Eighteen samples obtained from the core underwent analysis using the PANalytical X'Pert Pro diffractometer, equipped with an X'Celerator solid-state detector and a sample holder spinning, at Instituto Andaluz de Ciencias de la Tierra (CSIC-UGR). X-ray powder diffraction patterns were recorded using random oriented mounts with CuKα radiation, operated at 45 kV and 40 mA. Scans were conducted from 3° to 70° 2θ at 0.02° intervals. Mineral identification and semi-quantitative assessments of mineral abundance were derived through the utilization of the software Bruker EVA® and the minerals in the PDF-2 database. Semi-quantitative phase amount is based on the reference-intensity-ratio (RIR) method (Hubbard and Snyder, 1988) on basis of RIR values from database (Chung, 1975).

High-resolution elemental records were generated using X-Ray fluorescence (XRF) core scanner analyses on the sedimentary cores (Fig. 5). This was achieved using an Avaatech XRF Core Scanner at the XRF-Core Scanner Laboratory of the University of Barcelona, Spain. The core was scanned at a resolution of 0.5 cm, employing two distinct settings: 1) 10 s count times at 10 kV X-ray voltage and 650 μA X-ray current for light elements (Al, Si, P, S, Cl, Ar, K, Ca, Ti, Mn, V, Cr and Fe), and 2) 35 s count time at 30 kV X-ray voltage and 1700 μA X-ray current for heavy elements (Ni, Cu, Zn, Ga, As, Se, Br, Rb, Sr, Y, Zr, Nb, Au, Hg, Pb, Bi, Th and U in this case). Regular check points were subjected to triplicate analyses every 50 scans. Results were expressed in counts per second (cps) – intensity, and further normalized to the total sum of cps to mitigate the impact of water content, density variations, and sediment surface conditions (Bahr et al., 2014). Elements exhibiting low cps yield or noisy signals were excluded from the analysis. Subsequently, the centered log-ratio (clr) of the elements with high cps (Si, K, Ti, Fe, Mn, Rb, Zr, S, Ca, Sr, Br) was calculated. The clr transformation is a simple procedure that effectively removes the constant-sum constraint, the covariation of data when the proportion of one component changes affecting the proportion of the remaining component(s), from any compositional data and simultaneously retains their true covariance structure (Kucera and Malmgren, 1998). A principal component analysis (PCA) on these clr data was carried out using the Past 4.05 program (Hammer et al., 2001) to determine affinities between the different chemical elements (Fig. 6). Fig. 6 displays PCA correlation loadings and

Table 1
Age data for the LGA sedimentary sequence. Radiometric ages were calibrated using IntCal20.14c curve (Reimer et al., 2020) with Calib 8.2 (http://calib.org/calib/). Radiocarbon dates were analyzed at BETA Analytic laboratory (https://www.radiocarbon.com/). Plutonium analyses were carried out at Northern Arizona University, USA by Michael E. Ketterer.

ID	Real depth (cm)	Material	Conventional age	Median age cal BP	IRMS δ^{13}C
Surface	0			−69	
Pu	12,85			−13	
576,890	76,2	organic sediment	1360 +/- 30 BP	1289	−30,3
563,346	101,1	plant material	1370 +/- 40 BP	1293	−26,9
560,857	109,8	plant material	360 +/- 30 BP	414	−28,4
544,700	114,2	plant material	350 +/- 30 BP	396	−27,7
576,891	132,6	organic sediment	1940 +/- 30 BP	1864	−28,4
563,347	151	plant material	3890 +/- 30 BP	4333	−36,9
563,348	152,2	plant material	3090 +/- 30 BP	3295	−30,6
576,892	166,2	organic sediment	2210 +/- 30 BP	2230	−25,7
544,701	210,6	plant material	2140 +/- 30 BP	2128	−20,4
544,702	220,7	plant material	2660 +/- 30 BP	2769	−16,2
576,893	231,9	organic sediment	2740 +/- 30 BP	2823	−27,2
576,889	275,1	organic sediment	3060 +/- 30 BP	3277	−26,5

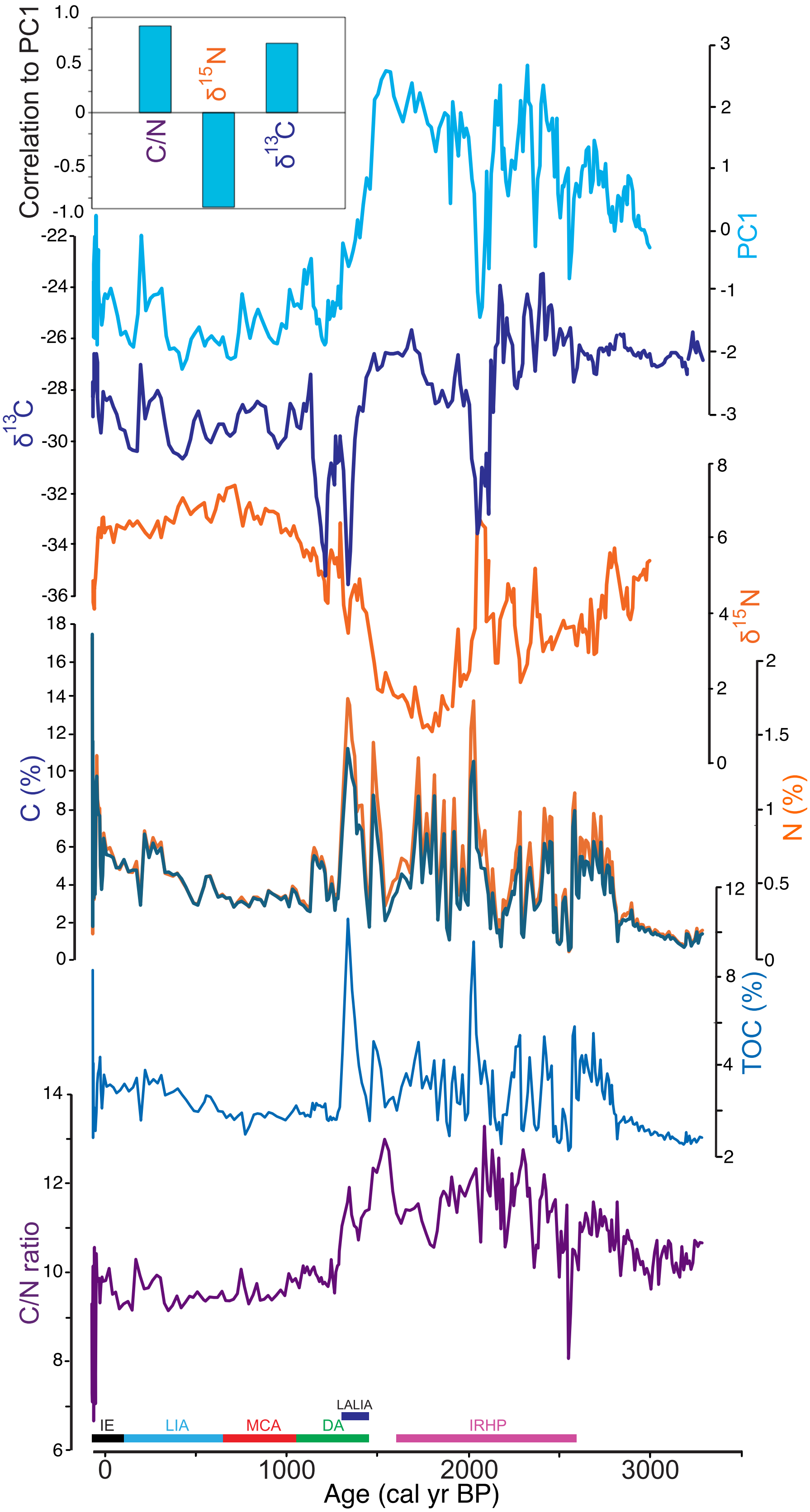

Fig. 3. Organic geochemistry data (from bottom to top C/N, TOC content, C, N, $\delta^{15}N$, $\delta^{13}C$, PC1 and correlation to PC1) of the LGA sedimentary record. The duration of historic periods such as the Iberian Roman Humid Period (IRHP), Late Antique Little Ice Age (LALIA), Dark Ages (DA), Medieval Climate Anomaly (MCA), Little Ice Age (LIA) and Industrial Era (IE) is indicated.

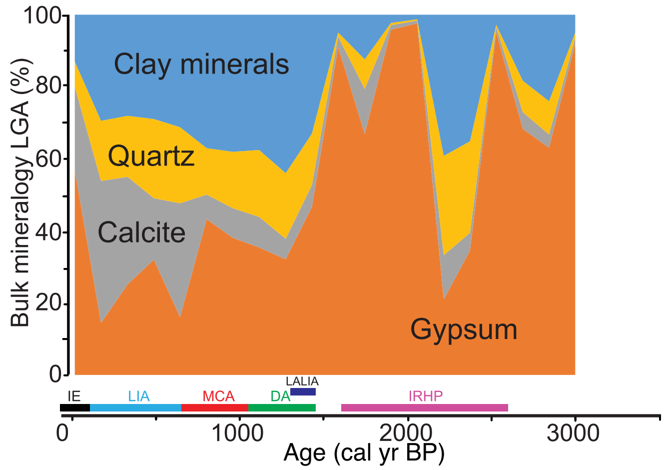

Fig. 4. Relative bulk mineral concentration from LGA sedimentary sequence obtained by XRD. The duration of historic periods such as the Iberian Roman Humid Period (IRHP), Late Antique Little Ice Age (LALIA), Dark Ages (DA), Medieval Climate Anomaly (MCA), Little Ice Age (LIA) and Industrial Era (IE) is indicated.

scatter biplot diagrams, providing a visual representation of the data's underlying structure. Several geochemical proxies measured by XRF scan, which have been proven to be good proxies for environmental change, were calculated (see discussion below), and a logarithmic (Napierian logarithmic; Ln) ratio transformation was done (Fig. 7). The log-ratios of element intensities offer the clearest insights into the relative shifts in chemical composition (Weltje and Tjallingii, 2008). In this study we selected and calculated the following ratios: Ln(S/Ti), Ln (Mn/Fe), Ln(Br/Ti), and Ln(Zr/Rb) (Fig. 7).

4. Results

4.1. Chronology

The $^{239+240}$Pu activity profile obtained in the topmost 20 cm of the LGA-19–04 core reached a maximum (2.5069 ± 0.067 Bq/kg) at 12.85 cm depth. The peak activity of $^{239+240}$Pu observed here can be attributed to a global fallout surge resulting from nuclear weapon testing, indicating an age approximately −13/-14 cal yr BP (1963/1964 CE) for this depth (Ketterer et al., 2004) (Table 1). The twelve AMS radiocarbon dates between 275 and 76 cm depth show age data between 4333 and 396 cal yr BP (Table 1). However, the Bayesian age-depth model of the LGA record indicates that the sediments span approximately the last 3300 cal yr BP and five dates show abnormal, either too young or too old, age results (Table 1; Fig. 2). An old carbon effect on the radiocarbon samples could have occurred but it is not considered here as the present-day lake water composition is calcium sulfated and shows low dissolved HCO^{3-} values, between 60 and 130 mg/l (Rodríguez-Rodríguez et al., 2001). The results obtained from the posterior log time series are stable and suggests a good fit. Following this age model, the average sedimentation rate of the record is 0.84 mm/year, although it is not constant throughout the record. The oldest section from 3280-2100 cal yr BP is characterized by a sedimentation rate of ∼ 1.08 mm/year (Fig. 2). The sedimentary rates in the section from 2100 to 1850 cal yr BP decreased to ∼ 0.82 mm/yr. The sedimentary rate further decreased later to ∼ 0.52 mm/yr from 1850-1400 cal yr BP. Between 1400 and 1100 cal yr BP the sedimentation rate increased to ∼ 1.13 mm/yr. The section between 1100–0 cal yr BP was characterized by sedimentation rates ∼ 0.55 mm/yr. The sedimentation rate from 0 (1959 CE) to −69 cal yr BP (2019 CE) was the highest ∼ 2.67 mm/yr.

4.2. Lithology and MS

The lithology of cores LGA 19–03 and LGA 19–04 is relatively homogeneous and mainly made up of clays and silts (Fig. 2). Greyish and light brown silty clays with the highest MS mostly characterize the bottommost part of the record from ∼ 276 (∼3280cal yr BP) to ∼ 204 cm (∼2600 cal yr BP). From ∼ 204 to 110 cm (∼1400 cal yr BP) brownish-greenish silts depicting the lowest MS values occurred. Greyish silty clays and an increase in MS characterize the sediments between 110 cm and the top (Fig. 5). Occurrence of nodular gypsum in sedimentary layers is observed mainly below 110 cm (1400 cal yr BP), where gypsum levels can reach several centimeters in thickness (Figs. 2 and 4). Gypsum is abundant between 267–258 cm and 204–110 cm (3200–3100 and 2600–1400 cal yr BP) and from 7 cm (−43 cal yr BP / 1993 CE) to the present (Figs. 2 and 4). Overall, low MS values are recorded during major occurrences of gypsum.

4.3. Organic geochemistry

The organic carbon content (Total Organic Carbon; TOC) varies significantly between 0.3 and 10.7 % in the LGA sediment record (Fig. 3). Low TOC values around 2.5 % are recorded between 276 and 226 cm (3300 and 2800 cal yr BP). The values then increased at around 4 %, reaching a peak of 5.8 % at 204 cm (2600 cal yr BP). Significant TOC oscillations are recorded between 204 and 100 cm (2600 and 1300 cal yr BP), with mean values around 3 % and two maxima of 9.7 and 10.7 % at 145 cm (2000 cal yr BP) and 104 cm (1350 cal yr BP), respectively. TOC values decreased considerably, and values around 2–3 % are registered between 100 and 3.5 cm (1300 and −53 cal yr BP). A very significant increase of more than 6 % is recorded between 3.5 cm

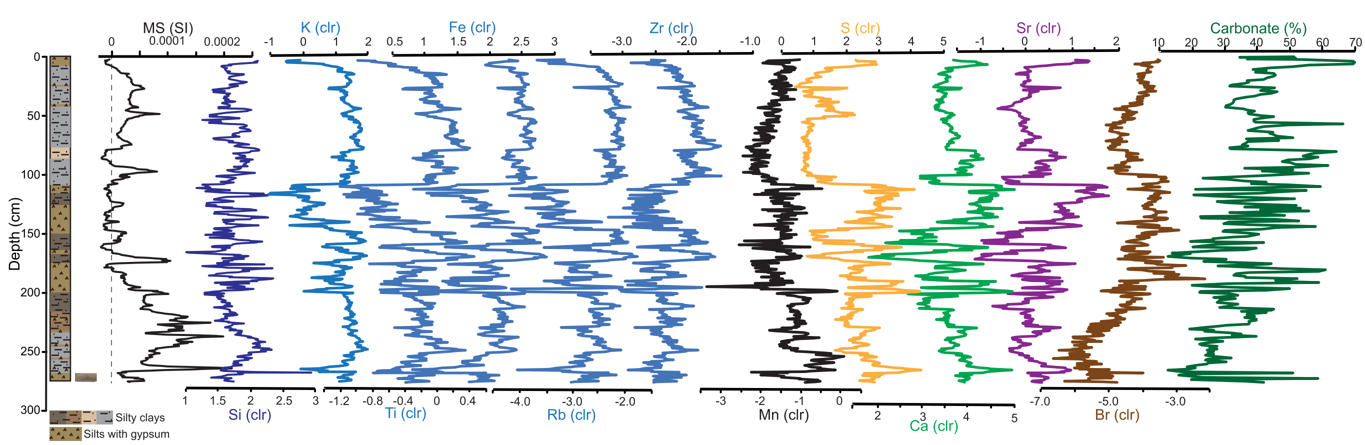

Fig. 5. Lithology, MS (in SI units), elemental XRF (clr) and carbonate data (in %) for the LGA composite sedimentary record.

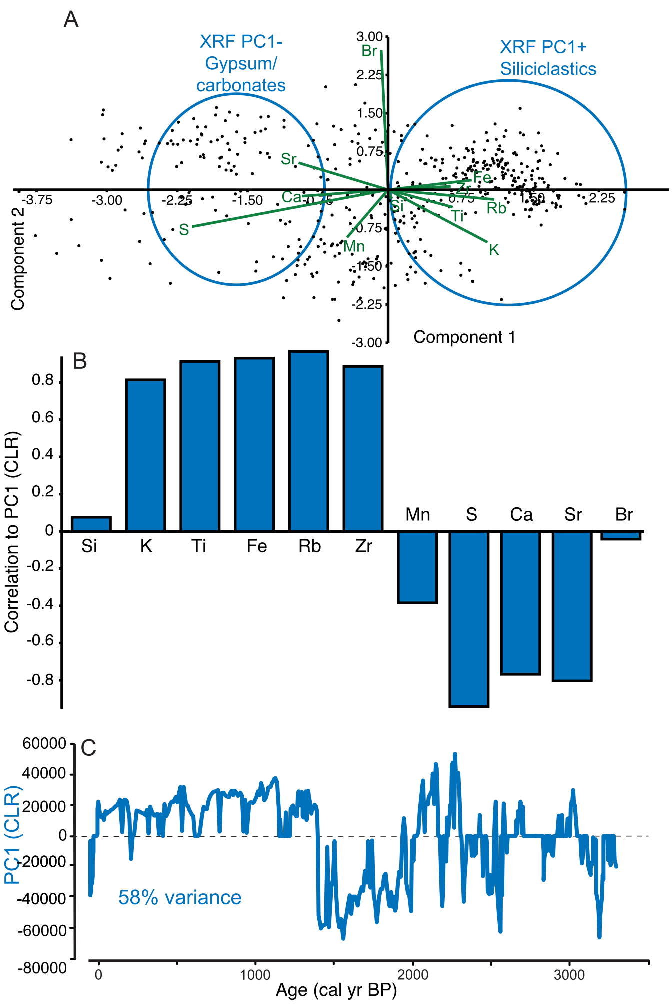

Fig. 6. PCA of the XRF data (clr) from LGA showing (A) the scatter plot with PC1 and PC2 axis variations, (B) correlation loadings of the different elements to PC1 and (C) PC2 and the PC1 (interpreted as siliciclastic vs evaporite content) (D) and PC2 (E) outcomes.

(−53 cal yr BP) (1953 CE) and present. C (%) and N (%) change in a very similar fashion to the TOC, showing the same long-term patterns and smaller-scale oscillations (Fig. 3).

The C/N atomic ratio (hereafter C/N ratio) range from 6.5 to 13.2 (Fig. 3). C/N values around 10.5 are recorded between 276 and 226 cm (3300 and 2800 cal yr BP). An increasing trend interrupted by several oscillations is observed between 226 and 154 cm (2800 and 2100 cal yr BP), with minima recorded at 199, 180 and 164 cm (2550, 2350 and 2200 cal yr BP). The highest value of 13.2 of the record is registered at 153 cm (2093 cal yr BP). Values are generally high but start a decreasing pattern with some variability between 153 and 100 cm (2100 and 1300 cal yr BP). Two peaks of around 13 and 12 occurred at 118 and 105 cm (1550 and 1350 cal yr BP), respectively. C/N ratio diminished considerably to values below 10 at 100 cm (1300 cal yr BP) and stayed low, generally around 10–9, until 6 cm (−44 cal yr BP; 1994 CE) when a sudden further decrease to the lowest value of 6.5 at 2.5 cm (−58 cal yr BP; 2008 CE) is observed.

δ^{13}C values oscillating between ~ -26 ‰ and −28 ‰ characterize the oldest part of the record between ~ 276 and 204 cm (3300 and 2600 cal yr BP; Fig. 3). Values increased later on, with three peaks ~ -24 ‰ at ~ 184, 174 and 163 cm (~2400, 2300 and 2200 cal yr BP). A minimum of –33.6 ‰ is recorded between ~ 153 and 149 cm (~2100 and 2050 cal yr BP) and values increased again between ~ 145 and 112 cm (~2000 and 1450 cal yr BP). A significant decrease occurred at 109 cm (1400 cal yr BP), reaching two minima of −35.5 ‰ and −35.2 ‰, the lowest values of the record, at 105 and 44 cm (1350 and 1200 cal yr BP), respectively. Values increased rapidly later on to mean values oscillating ~ -28 ‰ and −30 ‰ between 41 and 0 cm (1150 cal yr BP and present) with peaks of −28 and −27 between 17–14 cm (300–200 cal yr BP) and −28 and −26.5 at 9 cm (~0 cal yr BP (1950 CE)) and 2 cm (−58 cal yr BP (2008 CE)), respectively.

The δ^{15}N record is shorter than the δ^{13}C because some of the values, notably the values older than 3000 cal yr BP, failed to pass the quality control since their intensity fall below the linearity threshold of 600 mv for the mass 28 (Fig. 3). This record shows oscillating values but an overall decreasing trend between 248 and 131 cm (~3000 and 1800 cal yr BP), reaching then the minimum value of the record of 0.9 ‰. Interrupting this trend is a maximum peak above 6 ‰ between 153–149 cm (2100–2050 cal yr BP). δ^{15}N minima below 4 ‰ are reached between 145 and 112 cm (2000 and 1450 cal yr BP). Increasing values featuring a trend are recorded from then on until 27 cm (700 cal yr BP), when a peak ~ 7.5 ‰ is reached. δ^{15}N featured a decreasing trend from then on until 8 cm (−11 cal yr BP (1961 CE)) when a high-amplitude and sudden further decrease is observed until present and reaching values of ~ 4 ‰.

Organic geochemistry PC1 values explaining the ~ 70 % of the variance summarize the organic geochemistry data and show significant positive correlation to C/N and δ^{13}C with a pattern very similar to those two datasets recording maximum values between 184 and 109 cm (2400 and 1400 cal yr BP) (Fig. 3). Negative values characterize the rest of the record until a peak centered at ~ 3 cm (−53 cal yr BP (2003 CE)), when a positive value is recorded.

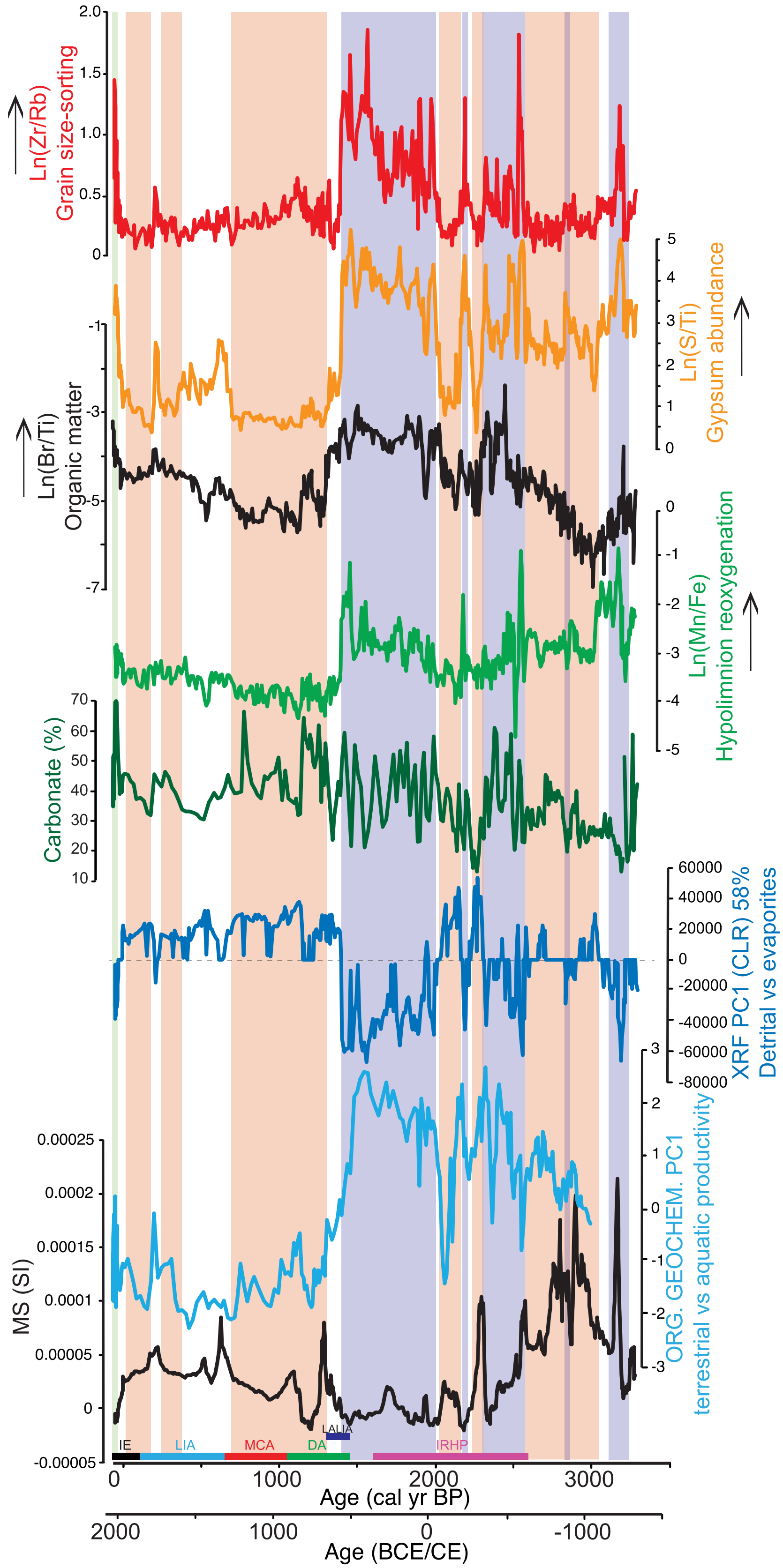

Fig. 7. Comparison of the XRF Ln(element/element) ratios, carbonate content, XRF PC1, Organic geochemistry PC1 and MS from the LGA record. The environmental interpretation of the elemental ratios and PC1s is written by their scale values. In light blue and pink color shadings are the identified humid and arid periods, respectively. In light green shading is the human impact period. The duration of historic periods such as the Iberian Roman Humid Period (IRHP), Late Antique Little Ice Age (LALIA), Dark Ages (DA), Medieval Climate Anomaly (MCA), Little Ice Age (LIA) and Industrial Era (IE) is indicated.

4.4. Inorganic geochemistry

4.4.1. Carbonate content

The carbonate content in the sedimentary record presents significant variability and oscillates between 10 and 70 % (Figs. 4 and 7). The bottommost part of the record is characterized by high carbonate content above 50 % between 274 and 269 cm (3260–3210 cal yr BP). The carbonate content drops to a minimum of around 10 % at 267 cm (3200 cal yr BP). The values then show an increasing trend peaking above 50 % between 198 and 189 cm (2550–2450 cal yr BP). Carbonate values dropped subsequently to a minimum of around 10 % at 170 cm (2260 cal yr BP). An increase in the values is then observed with several peaks above 50 % between 127 and 110 cm (2000 and 1600 cal yr BP). A minimum then is registered at 103 cm (1540 cal yr BP). Values increased again with two peaks above 60 % between 93–81 cm (1250–1150 cal yr BP). The values then dropped to around 30–50 % until present, with a peak above 60 % at 81 cm (1150 cal yr BP) and the maximum value of the record of almost 70 % between 7–4 cm (−40 – −55 cal yr BP; 1990–2005 CE).

4.4.2. Mineralogy

Bulk mineral composition was obtained by XRD in 18 representative selected samples along the sedimentary sequence of LGA (Fig. 4). The sediments sampled are predominantly composed by varying proportions of gypsum, calcite, quartz and clay minerals. Broadly speaking, and despite the low-resolution analysis, the samples can be categorized into three main distinct mineral compositions:

1) Samples predominantly composed of gypsum (>50 %) dating from 3200 to 1500 cal yr BP.

2) Samples predominantly by gypsum (~40 %) and clay minerals (>20 %), dating from 1500 to 630 cal yr BP.

3) Samples enriched in calcite (>15 %), dating from 630 to −49 cal yr BP.

Gypsum occurs in all samples (Fig. 4), albeit in varying concentrations. Notably, the first type of samples exhibits such a pronounced gypsum signal that it obscures the presence of other potential mineral phases, for this reason semiquantitive analysis only aims to show changes in gradients and domains in mineral abundances rather than absolute values with errors than can exceed 10 %.

4.4.3. Elemental composition

The elemental relative concentration was obtained using XRF-scan analysis (Fig. 5) and shows element variations in groups captured by the PCA and mostly explained by the PC1 (with a 58 % of the variance; Fig. 6), with a siliciclastic group (PC1 +) made up of Si, K, Ti, Fe, Rb and Zr covarying together and showing an opposite pattern of change than gypsum-carbonate components such as S, Ca, Sr and Mn (PC1-) (see loadings in Fig. 6B). The Si shows positive correlation to the siliciclastic PC1 + but with a low value (Fig. 6). The PC2, explaining the 23 % of the variance, is dominated by Br (PC2 +) versus Mn (PC2-) (Fig. 6A, 6D and 6E). Several Ln(element/element) ratios were also calculated and show variations that are mostly related to the lithological changes (Fig. 7). The signals of V, Cr, Ni, Cu, Zn, and Pb obtained from the XRF analysis are very low.

In summary, the last ~ 3300 cal yr BP in the LGA sedimentary record are characterized by three main gypsum intervals depicted by minima in elements PC1+, and maxima in Ln(Br/Ti), Ln(S/Ti), Ln(Zr/Rb) and Ln (Mn/Fe) ratios (Fig. 6). The first gypsum-rich period is observed from 268-258 cm (3200 – 3100 cal yr BP). The second one is from 204-110 cm (2600 – 1400 cal yr BP), interrupted by two more detrital events between 173–164 and 159–149 cm (2300 – 2200 and 2150 – 2050 cal yr BP). The third period is located from 12.5 to 0 cm (−15 – −69 cal yr BP). The main detrital (PC1 +) intervals are observed (1) between 253–204 cm (3050 – 2600 cal yr BP) interrupted by short gypsum-rich event around 230 cm (2830 cal yr BP); (2) between 100–53 (50) cm (1300 – 700 (650) cal yr BP) and (3) between 35–18 cm (350 – 50 cal yr BP), interrupted by a short relative gypsum-rich interval at around 26 cm (200 cal yr BP).

5. Discussion

In this study we observe changes in the sedimentation with mineralogical and geochemical variations at LGA for the last ~ 3000 years, which were mostly controlled by factors including climate, biological activity and anthropogenic perturbation. 1) Climate affects sedimentation through changes in precipitation and temperature influencing lake level and water column oxygenation, hydrology or erosion/runoff in the drainage basin. 2) Biological activity including the growth and decay of aquatic organisms, such as mollusks, plants and algae, can affect sedimentation. Allochthonous terrestrial organic matter and organic matter produced by biological activity accumulate together with mineral particles, including authigenic carbonates, influencing sediment composition. Aquatic productivity, and thus organic matter accumulation might be also enhanced by warm climate. In addition, high organic matter at the lake bottom and water column stratification during humid/warm periods can promote periodic dysoxic hypolimnion conditions (Naeher et al., 2013). In addition, during humid periods an increase in lakes solutes from groundwater also could favor gypsum precipitation. 3) Anthropogenic activities comprise human perturbations such as agriculture, deforestation, dredging, groundwater withdrawals, nutrient loading and recent global warming, which can directly impact sedimentation processes in lakes. Agriculture and deforestation in the catchment area can accelerate erosion and sedimentation rates, while nutrient inputs can fuel algal blooms that contribute to organic input and oxygen levels decrease, affecting sedimentation. Below are the main sedimentological signals (i.e., climate/environmental proxies) identified at the LGA record and the possible factors controlling their changes through time.

5.1. Proxy interpretation of the LGA sedimentary record

5.1.1. Detrital and authigenic signatures

MS data indicate the amount of magnetic minerals within the sediments deposited at LGA (Fig. 6). In this area, the magnetic minerals are mostly found in the siliciclastic rocks and thus MS can be used here as a proxy for siliciclastic detrital input or content in the lake sediments due to changes in the erosion rate, productivity and/or evaporite deposition. However, another source of magnetic material could be biogenic magnetite (Byrne et al., 2016). Biogenic magnetite refers to magnetite (Fe_3O_4) that is produced biologically, often by organisms such as magnetotactic bacteria or certain animals (Amor et al., 2015).

The concentrations of Si, K, Fe, Rb, Ti, and Zr in sedimentary deposits typically originate from siliciclastic detrital materials, predominantly linked to erosive processes (Kylander et al., 2011). Ti and Zr typically indicate relatively coarse and heavy grains, whereas Rb predominantly associates with finer and lighter sediment fractions (Kylander et al., 2011; Olivares-Casillas et al., 2021). This is because Zr is mainly found in heavy minerals such as zircon ($ZrSiO_4$), usually depicting a relatively coarse grain-size, because it is hard, stable, and resistant to physical and chemical weathering (Hasan et al., 2022). With its high sorption capacity in clay minerals, Rb displays low mobility but also substitutes for K in feldspars of variable grain size (Kylander et al., 2011) and is mainly found in K-rich minerals, such as mica, illite, and K-feldspar (Dypvik and Harris, 2001). The positive correlation observed between K and Rb in LGA's sediments ($r = 0.87$; $p < 0.01$; see Figs. 5 and 6) suggests their association with the influx of fine material into the sedimentary deposit. Therefore, the Ln(Zr/Rb) ratio derived from XRF core scanning holds potential as a high-resolution tracer for grain-size variations of sediments, and hence sediment sorting (Wu et al., 2020; Fig. 7).

The low positive correlation of Si with other siliciclastic elements of the PC1 + group (Fig. 6) suggests that there should be a different factor controlling its abundance in the LGA sediments. Ln (Si/Ti) data covary with Ln(Zr/Rb) ratios, indicating that well-sorted sediments are rich in Si that most-likely originates from quartz grains.

Conversely, Ca, S and Sr concentrations in lacustrine sediments, mainly associated to carbonate/evaporite minerals can result from authigenic precipitation and/or clastic input due to the erosion of materials from the drainage basin (Algeo and Liu, 2020; García-Alix et al., 2022). Evaporite precipitation occurs when dissolved cations in water reach saturation concentrations, facilitated by physical, chemical, and biological processes leading to their deposition on the lake floor (Cohen, 2003). The LGA record shows negative correlations between detrital elements (Ti and Zr) and Ca, S and Sr (Figs. 5 and 6) indicating that the latter elements predominantly originate from biologically mediated and/or from authigenic carbonate and sulfate precipitation. A potential source of carbonates could originate from biogenic precipitation from gastropods or charophyte algae (Camuera et al., 2018), which also occur in the LGA sediments. At present, gypsum has been observed to form at the LGA subaerial margin and floor. The authigenic gypsum can be obtained by the Ln (S/Ti) ratio, because Ti is found mainly in detrital input allowing to substract S increase associate to a higher detrital gypsum input (Fig. 7).

Summarizing, the detrital versus evaporite/biogenic sedimentary changes in the LGA sedimentary sequence is shown by the PCA of the geochemical data, with most positive PC1 values generally indicating a higher content of detrital sediments, while the most negative PC1 values would mostly correspond to evaporite/carbonate sedimentation (Fig. 6). The negative correlation between PC1 + and the grain size proxy Ln(Zr/Rb) indicates the bigger grain size/sorting of the detrital fraction during the more evaporite phases (Fig. 7).

5.1.2. Organic matter source and lake productivity

The amount of organic matter in the sediments from LGA, indicating organic matter input and/or lake productivity is revealed by the TOC values and indirectly by the Ln(Br/Ti) ratio. The positive correlation ($r = 0.51$; $p < 0.01$) between TOC and Ln(Br/Ti) in the LGA sediment core confirms this relationship. Previous studies found a positive relationship between Br and the amount of organic matter in lake sediments (Leri and Myneni, 2012; Guevara et al., 2019). Leri and Myneni (2012) suggested that inorganic Br undergoes transformation into organic compounds within forest soils during the decay of vegetal remains, facilitated by enzymatic processes. As plants absorb inorganic Br during growth, this Br is subsequently converted into organic forms as the plant remains decomposes. These organic Br compounds become integrated into the soil organic matter matrix (Leri and Myneni, 2012). Subsequently, organic matter inputs from the catchment area to lakes carrying organic Br, which circulates within the water body and becomes incorporated into sediments. Therefore, the Ln(Br/Ti) ratio could be useful in order to distinguish between authigenic and detrital organic matter input as Br has a terrestrial source. The positive correlation between Br and TOC has also been observed in other sedimentary records from the southern Iberian Peninsula in the Gulf of Cadiz (Bahr et al., 2014) or Padul wetland (Camuera et al., 2018). The little correlation between Br and S (Figs. 5 and 6) indicate that S is controlled mainly by the presence of gypsum instead of organic matter as described in other Iberian Peninsula lakes (Vegas-Vilarrúbia et al., 2018).

The C/N ratio from the LGA record offers insights into the historical dynamics of organic matter sources spanning the past 3300 cal yr BP in the lake (Fig. 3). Freshwater algae exhibit a distinctive nitrogen enrichment with a carbon depletion compared to vascular plants. Consequently, a low atomic C/N ratio in organic sediments indicates a prevalence of algae (C/N < 10), whereas high ratios (C/N > 20) suggest an abundance of external vascular plant material (rich in cellulose and poor in protein). Intermediate values (C/N ratio between 10 and 20) indicate a mixed influence of both sources (Meyers, 1994; Meyers and Teranes, 2001). The positive correlation between C/N and Br/Ti ratios ($r = 0.57$; $p < 0.01$) indicates that abundant organic matter (high Br/Ti ratio) is primarily of terrestrial origin (high C/N ratio). There exists a moderate positive correlation between the carbonate content and C (%) and N (%) ($r = 0.40$ and 0.46, respectively). This could suggest that, at least partially, the carbonate has a biogenic source, occurring during moments of enhanced lake productivity. The δ15N and δ13C records serve as valuable indicators for identifying organic matter sources and assessing productivity levels (Meyers, 2003). The δ13C record from organic matter at LGA, ranging from −35.5 ‰ to −24.0 ‰, aligns with the typical isotopic composition of C3 plants (O'Leary, 1981, 1988; Meyers, 1994). However, samples with the highest isotopic values likely also reflect contributions from phytoplankton (Galimov, 1985), as supported by the intermediate atomic C/N ratios. Parallel variations of C/N and δ13C usually mark fluctuations in the source of organic matter (external inputs or local algal productivity) (García-Alix et al., 2012). Higher aquatic productivity often increases δ^{15}N levels in sediment because of greater biological nitrogen uptake and recycling (Brenner et al. 1999; Talbot and Laerdal, 2000; Teranes and Bernasconi 2000). Terrestrial organic inputs into the system would also deplete the sedimentary δ^{15}N values (McLauchlan et al., 2013). In recent times, shifts in the sedimentary δ^{15}N signal towards lower values can be also a consequence of anthropogenic local activities, such as fertilizer runoff inputs from cultivation, and/or regional/global sources due to atmospheric isotopic changes caused by fertilizer production or fossil fuel combustion, among others (Enders et al., 2008; Holtgrieve et al., 2011).

5.1.3. Redox dynamics

The Mn concentration is subject to the dynamic interplay of reduction and oxidation processes following deposition (Makri et al., 2021). In oxygen-rich conditions within the water column, Mn precipitates within sediments as oxyhydroxides of manganese (Makri et al., 2021). Conversely, under dysoxic to anoxic conditions, Mn redissolve re-entering the water column (Algeo and Liu, 2020). Originating from detrital sources, an unaltered signal of this element would typically exhibit positive associations with detrital elements less susceptible to post-depositional alteration. However, in our dataset, Mn shows decoupling from Fe, Ti and Zr concentrations, indicating significant variance attributable to post-depositional processes. The Ln(Mn/Fe) ratio has been previously used as a redox-sensitive proxy to reconstruct bottom water oxygenation in lakes (Naeher et al., 2013), with high Ln (Mn/Fe) ratio pointing to the preservation of redox fronts during lake water stratification and low oxygen hypolimnion (Makri et al., 2021; Neugebauer et al., 2022; Vizcaino et al., 2022). Consequently, we interpret Ln(Mn/Fe) ratio enrichments at LGA as post-depositional migrations of the redox front and reoxygenation and reoxidation of the surface sediment layers linked to major changes in hypolimnion oxygen conditions between summer (dysoxic) and winter (oxygenated) during humid/warm periods (Algeo and Liu, 2020). The oxygen depletion during summer could have been produced by higher lake levels and/or higher productivity and/or longer thermal stratification. The negative correlation between Ln(Mn/Fe) and PC1 + indicates the presence of these periodical low oxygen conditions and the reoxygenation of the lake bottom during the deposition of evaporites at LGA.

5.2. Main environmental and climatic trends during the last 3300 cal yr BP in the western Mediterranean conditioning sedimentation in LGA

5.2.1. The period between 3300–2600 cal yr BP

Overall low lake level and dry climate conditions are interpreted for the LGA record at that time (Figs. 7 and 8). This is deduced from the generally low organic matter content (TOC, Br/Ti) and thus low lake productivity, and high MS (Fig. 7), suggesting more erosion and slightly more detritic input (PC1 +) in the lake, specially between 3050–2600 cal yr BP. This agrees with other regional studies showing low forest cover during that period (Jiménez-Moreno et al., 2015, 2022; Ramos-Román et al., 2016, 2018; Mesa-Fernández et al., 2018) (Fig. 8), which could have triggered desertification and enhanced soil erosion at LGA. Little influence of terrestrial organic matter source on the LGA sediments

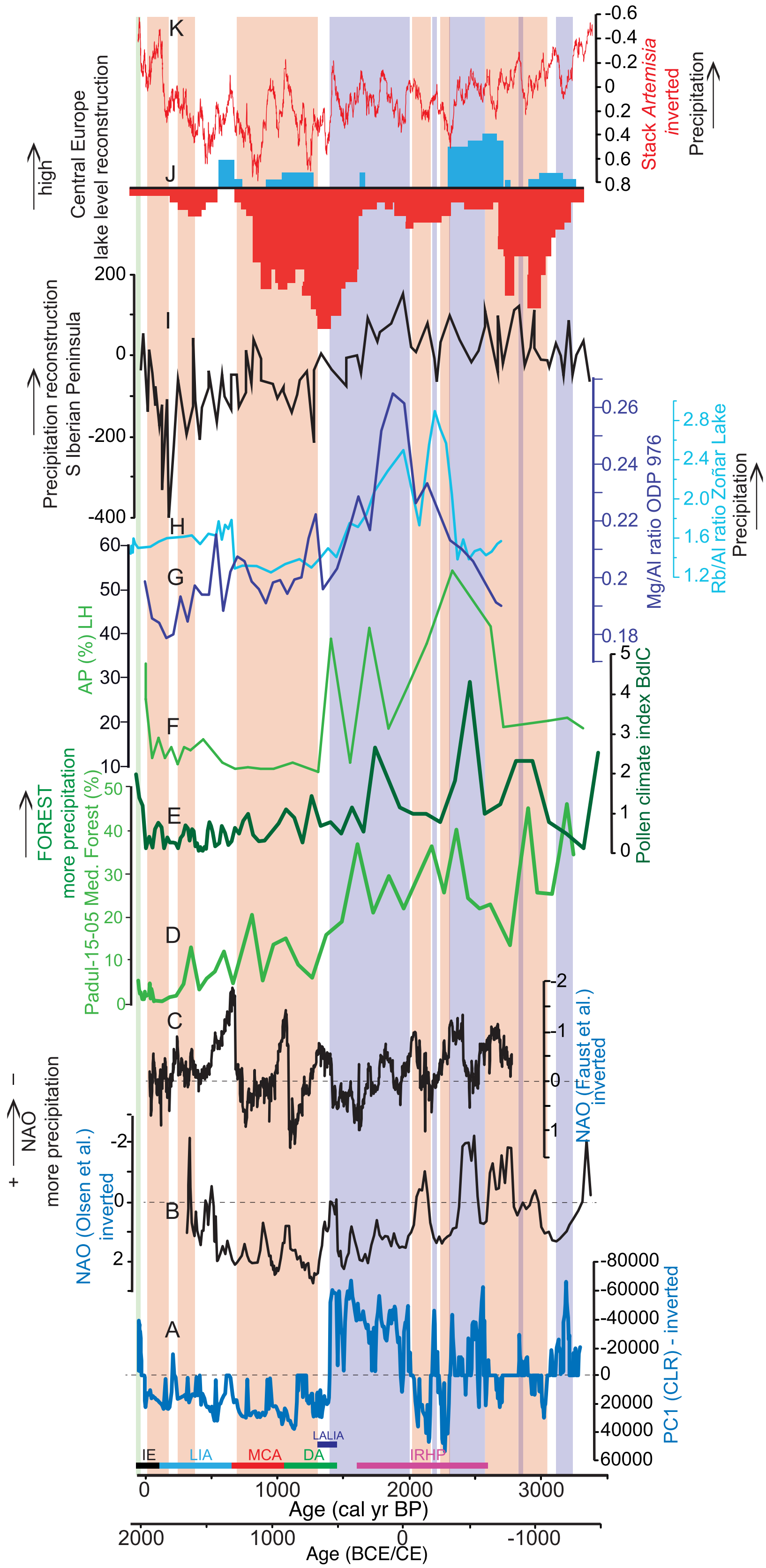

(caption on next page)

Fig. 8. Comparison of the XRF PC1 record from LGA with other regional and global records of paleoprecipitation. (A) PC1 of LGA XRF (note that it is inverted). (B and C) NAO reconstructions (Olsen et al., 2012; Faust et al., 2016). (D) Padul-15–05 Mediterranean forest (%) (Ramos-Román et al., 2018). (E) Pollen climate index from Borreguil de la Caldera site, Sierra Nevada (Ramos-Román et al., 2016). (F) Percentage of arboreal pollen (AP) from Laguna Hondera, Sierra Nevada (Mesa-Fernández et al., 2018). (G) Mg/Al ratio from site ODP 976, Alboran Sea (Martín-Puertas et al., 2010). (H) Rb/Al ratio from Zoñar Lake, Córdoba (Martín-Puertas et al., 2010). (I) Precipitation reconstruction from S Iberian Peninsula based on pollen records (Ilvonen et al., 2022). (J) Lake-level reconstruction for central Europe (Magny, 2004). Low and high lake levels are represented in red and blue, respectively. (K) Stack of Artemisia xerophyte from Iberia and Morocco (inverted) (Camuera et al., 2023). In light blue and pink color shadings are the identified humid and arid periods, respectively. In light green shading is the human impact period. The duration of historic periods such as the Iberian Roman Humid Period (IRHP), Late Antique Little Ice Age (LALIA), Dark Ages (DA), Medieval Climate Anomaly (MCA), Little Ice Age (LIA) and Industrial Era (IE) is indicated.

is also confirmed by the low C/N (ranging from 10 to 12) and relatively high $\delta^{15}N$ values (Fig. 3), suggesting relatively less dense vegetal coverage in the catchment during this period. The erosion of the most vegetation-devoid soils around the lake could be facilitated by a stormier climate characterized by unevenly distributed rainfall events throughout the year, typical of a Mediterranean climate.

Aridity between 3300 and 2600 cal yr BP is corroborated by multiple previous studies. Firstly, an approximately 3000 cal yr BP arid event, identified locally through the desiccation of Laguna de Medina (Reed et al., 2001), and the deposition of eolian deposits around 2700 cal yr BP in the SW Iberian coastal region (Zazo et al., 2005). Additionally, this phenomenon has been regionally observed through lowered levels in Zoñar and Siles Lakes (Carrión, 2002; Martín-Puertas et al., 2008), as well as documented geomorphic instability in the area (Bellin et al., 2013). Furthermore, this dry temporal interval aligns with decreased lake levels across central Europe (Magny, 2004; see Fig. 8). Enhanced aridity at this time could have been due to persistent positive NAO conditions (Olsen et al., 2012; see Fig. 8), typically resulting in a general decrease in winter precipitation in the area (Trouet et al. 2009).

The LGA sedimentary record also shows some rapid time-scale variability during this period. The overall dry period was interrupted between ~ 3200–3100 cal yr BP by presumed relatively more humid period, that resulted in higher groundwater discharge and gypsum precipitation, greater primary production in the lake, larger grain size

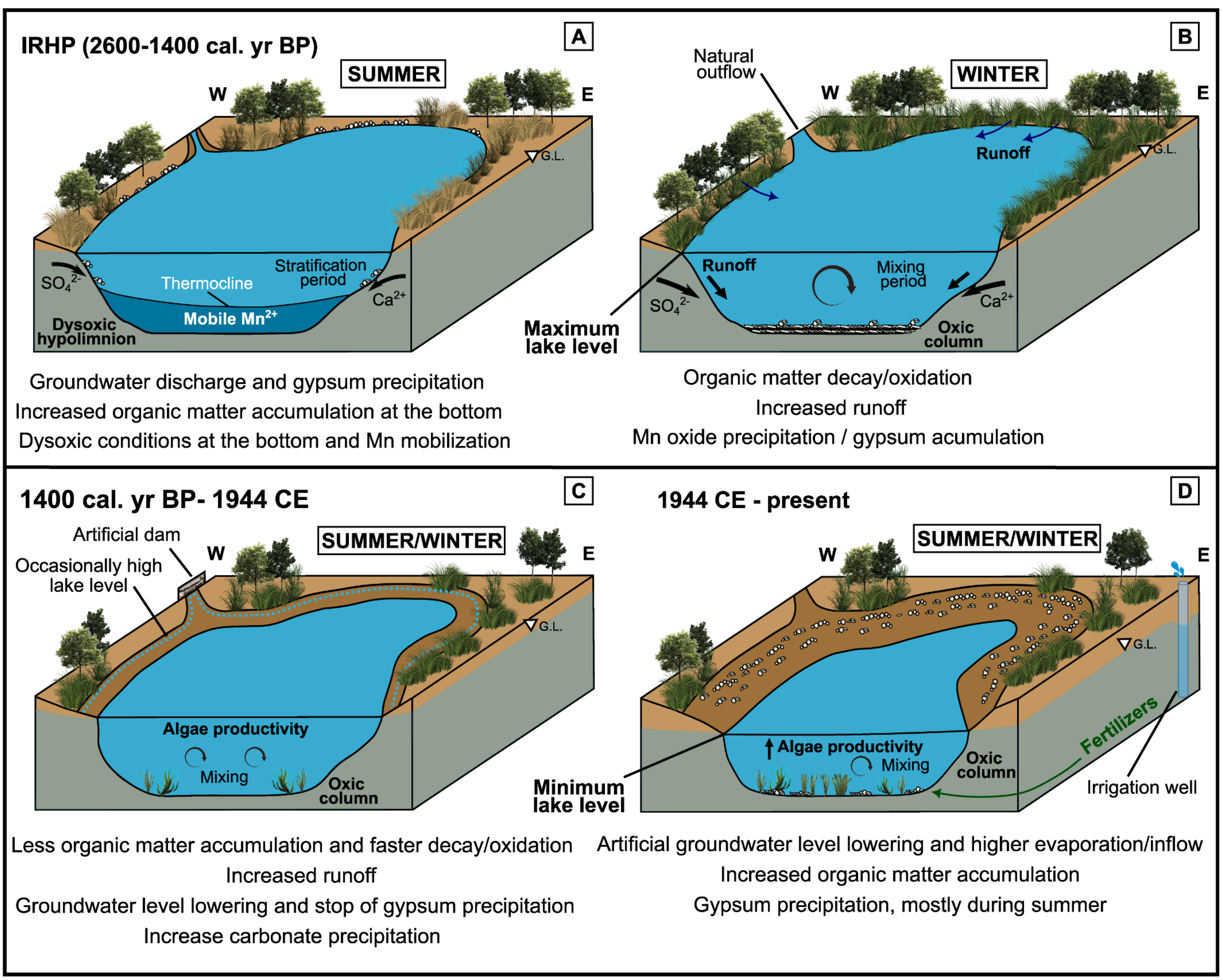

Fig. 9. Schematic evolution of LGA during the last 3300 cal yr BP. (A) During summer conditions of the IRHP (2600–1400 cal yr BP) at highest lake levels. (B) Winter conditions during the IRHP at highest lake levels. (C) LGA lake between 1400 cal yr BP and 1944 CE. (D) LGA in the last decades and since 1944 CE when the lowest lake level conditions occurred.

and enhanced sorting, and more redox events lake water, deduced by maxima in Ln(S/Ti), Ln(Br/Ti), Ln(Zr/Rb) and Ln(Mn/Fe) ratios, respectively. A shorter and less humid period was centered at ~ 2830 cal yr BP (Figs. 6 and 7).

5.2.2. The wet Iberian Roman humid period between 2600–1400 cal yr BP

The highest lake level and most humid and productive period, coinciding with enhanced terrestrial organic matter content, gypsum precipitation, sediment sorting at LGA occurred between 2600 and 1400 cal yr BP, deduced by minima in MS and XRF PC1 + elements and maxima in Ln(S/Ti), Ln(Br/Ti), organic geochemistry PC1 and Ln(Zr/Rb) ratios (Figs. 7-9). In addition, the Ln(Mn/Fe) ratio generally shows higher values between ~ 2600 and 1400 cal yr BP. This probably indicates alternating oxygenated and dysoxic conditions at the bottom waters of this warm monomictic lake during a period of high lake levels (i.e., lake stratification and dysoxic conditions in summer and water column mixing and oxygenation in winter). The enhanced humidity played a significant role in promoting the substantial growth of terrestrial vascular plant cover evident in LGA during the IRHP until approximately 1300 cal yr BP, as indicated by peak values in the C/N ratio and TOC content and minima in $\delta^{15}N$ (Fig. 3). The relatively high TOC content during this period seems to be closely related to gypsum precipitation (see section 5.2.2.1 below), which does not seem to have formed in LGA during the driest period of the record.

The IRHP in the southern Iberian Peninsula, including the Roman Empire's rule in this region, has been widely studied by various authors (Martín-Puertas et al., 2008, 2009, 2010; Jiménez-Moreno et al., 2013, 2015, 2022; García-Alix et al., 2022; Gázquez et al., 2020, 2023). Increased humidity is evidenced by elevated lake levels across southern Spain and central Europe (Magny et al., 2004; Martín-Puertas et al., 2010), a conclusion supported by additional precipitation proxies such as Mg/Al and Rb/Al ratios from site ODP 976 in the Alboran Sea and Zoñar Lake, southern Spain (Martín-Puertas et al., 2010). These proxies indicate a rainfall peak during this period, which agrees with the highest estimated precipitation values of the last three millennia obtained from pollen records from S Iberia (Ilvonen et al., 2022; Fig. 7). The prevailing humid conditions in the Mediterranean region during the IRHP have been attributed to elevated winter rainfall, likely originated by persistent negative NAO conditions, as suggested by Olsen et al. (2012) (Fig. 7) and warmer Mediterranean Sea surface conditions (about + 2°C) (Margaritelli et al., 2020). However, generally humid conditions were interrupted by brief intervals of aridity as observed in lake sediments (Martín-Puertas et al., 2009; Gázquez et al., 2023), caves (Gázquez et al., 2020), and marine sediment records from the Alboran Sea (Martín-Puertas et al., 2010; Nieto-Moreno et al., 2011; Rodrigo-Gámiz et al., 2011). At LGA, the generally humid period was also interrupted by two arid events between 2300–2200 and 2150–2050 cal yr BP, indicated by maxima in MS, clay minerals content and XRF PC1 + elements, and minima in Ln(Br/Ti), organic geochemistry PC1+, Ln(S/Ti) and Ln(Zr/Rb) ratios (Figs. 3, 4, 7 and 8). The latter could be linked to a synchronous aridity event described in Lake Zoñar between 2120–2050 cal yr BP (Gázquez et al., 2023).

The end of the exceptionally humid phase at LGA, which stands as one of the most humid periods documented in our record, aligns temporally with the Late Antique Little Ice Age (LALIA), documented elsewhere from approximately 500 to 650 CE (1450 – 1300 cal yr BP) (e.g., Büntgen et al., 2016). This period is likewise marked by humid (and cold) conditions, as noted by Bartolomé et al. (2024). Historically, the vanishing of the Roman rule of Iberia and the overtake of the region by the Visigoths (~500 CE) coincides with the transition to a drier period during which olive cultivation areas were reduced (Ramos-Román et al., 2019).

5.2.2.1. Gypsum precipitation during the IRHP and in recent times.

Gypsum occurred consistently and is especially abundant in the LGA record during the IRHP wet period between 2600–1400 cal yr BP [Ln(S/Ti) ratio in Figs. 7 and 9B, and %gypsum in Fig. 4]. Therefore, gypsum precipitation at LGA does not seem to be linked to more evaporative conditions as a result of arid climate conditions, contrary to interpretations from other Iberian lakes (Martín-Puertas et al., 2008, 2009; García-Alix et al., 2022; Gázquez et al., 2023) and elsewhere (Hodell et al., 2008; Evan et al., 2008).

Gypsum occurs in the LGA record during periods of high humidity, indicated by the higher grain-size/sorting, and catchment/lake productivity, as indicated by high TOC content and Ln(Br/Ti) values, during the IRHP and from the second half of the 20th century to the present. A potential explanation for the occurrence of gypsum during the IRHP can be attributed not to an increase evaporation but rather to groundwater levels rising during this wetter period. An increase in Ca^{2+}-SO_4^{2-}-rich water inlet from the aquifer could lead to gypsum precipitation during this warm/humid climate stage. In this sense, Mediavilla et al. (2020) noted that the paleo-salinity signature in a saline lake from the "Lagunas Reales" in Central Spain was not attributed to increased evaporation but rather to groundwater levels rising during wetter periods of the Holocene. A similar model has been used to explain the increase in water salinity in Laguna de Medina (southwestern Spain) during wetter period of the Holocene (Reed et al., 2001). However, the Lagunas Reales and Laguna de Medina are quite different lakes from LGA, as they are much shallower (generally with maximum lake levels between 0.5–2 m) and ephemeral at present, suggesting they have remained dry for long periods. In such circumstances, it appears that the aforementioned model accounts for complete hydrological shift from wetter periods, when the lakes receive saline groundwater discharge, to the arid phases, in which the wetlands act as brackish evaporative water body that is virtually disconnected from the aquifer. This explains the "counterintuitive" increased salinity patterns observed there and in other parts of the world during humid periods (Parsons et al., 2002).

An additional mechanism to explain gypsum precipitation during the IRHP could have been associated with an increase in terrestrial organic matter input. Organic matter increase and subsequent decay could have produced recurrent dysoxic conditions at the lake bottom during the IRHP resulting in slightly lower water/sediment pH that could have hindered carbonate precipitation and/or preservation, favoring gypsum precipitation. Such a mechanism can also explain gypsum precipitation in recent times, when organic matter increased, in this case because anthropic factors (see section below). However, water data measured between 1997 and 2001 show that salinity (electrical conductivity: EC and total dissolved solids: TDS) increased when the lake level dropped due to less precipitation and more evaporation (Rodríguez-Rodríguez et al., 2007; Fig. 1E). A similar pattern was observed between 2014 and 2015 (Gil-Marquez et al., 2016) and more recently between 2019 and 2024 (unpublished data). In summary, increase in productivity and very low lake levels triggering higher evaporite concentration at LGA could have been the key factor for recent gypsum precipitation, in contrast to the IRHP, when gypsum precipitation was mostly controlled by increased input of Ca^{+2}-SO_4^{2-} – rich water to the lake due to groundwater level rising (Fig. 9).

5.2.3. The dry Dark age and Medieval climate Anomaly between 1400–650 cal yr BP (550—1300 CE)

The LGA geochemical data indicate variability but overall low lake levels and arid conditions between 1300–700 cal yr BP (650 – 1200 CE), during most of the DA and MCA. This is interpreted from the increase in MS and the PC1 + elements, suggesting more erosion (less vegetation development in the catchment, thus less soil retention) and more detrital input (PC1 +), but also from the lower terrestrial organic input (minima in C/N, organic geochemistry PC1 + and Ln(Br/Ti) ratios and TOC content) and thus lower but more aquatic lake productivity (higher $\delta^{15}N$) (Figs. 3, 7 and 8). The Ln(Mn/Fe) ratio also decreased at 1400 cal yr BP and depicts very low values during this period (Fig. 6) most-likely pointing to annually well-oxygenated lake water column. Calcite precipitation, indicated by the mineralogical content (Fig. 4) and % carbonates (Fig. 7), generally enhanced at this time in the LGA, which could have been due to increased authigenic precipitation under lowered lake levels or due to more biogenic calcite productivity (e.g., charophytes, gastropods) in the lake.

We suggest that the cessation of gypsum precipitation during this period was due to a lower input of saline water from the aquifer compared to previous periods (e.g., IRHP). This would have been a consequence of the decline in the water table level in relation to a decrease in the amount of rainfall, reinforcing the idea of relatively dry conditions during the DA and MCA (Fig. 9C). A higher rainfall/groundwater input ratio may have contributed to some water freshening during this period compared to the precedent IRHP (Fig. 9). Also, gypsum precipitation was likely hampered by other biochemical processes occurring in the lake, even though the lake level was lower than during the IRHP. We hypothesize that conditions during this low lake level period could have favored the precipitation of carbonates over gypsum due to a pH increase related to a lower input of terrestrial organic matter and the decrease in decay/oxidation (Fig. 8C). Calcite precipitation due to a pH increase and HCO_3^- inputs has been demonstrated to inhibit gypsum precipitation and even contribute to gypsum dissolution in calcium-sulfate rich environments like gypsum karsts (Forti and Rabbi, 1981), gypsum-rich soils (Al-Barrak and Rowell, 2016), and aquifers (Jin et al., 2010). This mechanism is attributed to the common-ion effect that favors the precipitation of the less-soluble calcite over the more soluble gypsum when forming from Ca^{+2}-HCO_3^--SO_4^{2-}-rich waters (Wigley, 1973). Water level decline could have also benefited the growth of charophyte algae on the lake bottom, as they thrive in shallow lakes permitting their photosynthesis (Choudhury et al., 2019). Charophytes, which are abundant in LGA at present, have been shown to be efficient in the nucleation and precipitation of carbonates in lakes (Anadón et al., 2000). For example, charophytes may contribute several hundred grams of $CaCO_3$ per square meter in the littoral lake bottom per year and, in some cases, $CaCO_3$ may constitute 70 % of their composition (Anadón et al., 2000 and references therein). Enhanced algae production in the LGA during the DA and MCA is supported by coupled decreasing/increasing trends in the sedimentary C/N and $\delta^{15}N$ records, respectively.

Several lines of evidence suggest that after the IRHP, climate in the southern Iberian Peninsula depicted a trend towards aridification and overall arid conditions occurred during the DA and MCA. For instance, the arid conditions prevailing during this period are clearly indicated by the decline in forest species and estimated precipitation observed in pollen records throughout the region (Ilvonen et al., 2022; Fig. 7). This forest decline is notable in areas such as the Doñana area (Jiménez-Moreno et al., 2015), the Guadiana Valley in Portugal (Fletcher et al., 2007), and the Padul and Sierra Nevada regions (Ramos-Román et al., 2008; Mesa-Fernández et al., 2018; Jiménez-Moreno et al., 2013; 2022). Similar trends are also evident in the Alboran Sea records, as indicated by cores MD95-2043 and ODP 976 (Combourieu Nebout et al., 2009; Fletcher et al., 2013). Noteworthy desiccation events during this period are recorded in Laguna de Medina (Reed et al., 2001). Moreover, reductions in Mg/Al and Rb/Al ratios in the Alboran Sea and Lake Zoñar suggest decreased precipitation (Martín-Puertas et al., 2010), and gypsum speleothems stopped growing in the southeastern Iberian Peninsula at ~ 1200 cal yr BP because of decrease in cave water seepage (Gázquez et al., 2020). Simultaneously, lake levels in southwestern and central Europe notably lowered (Magny, 2004; Martín-Puertas et al., 2010). In a recent study, Camuera et al. (2023) also showed significant droughts between the mid-5th and mid-10th centuries CE (450–950 CE), especially at 695–725, 755–770, 900–935 and 1075–1140 CE (Fig. 7). Paleoclimatic reconstructions show that a persistent positive mode of the NAO most likely dominated this period (including the MCA; Trouet et al., 2009; Moreno et al., 2012; Olsen et al., 2012; Baker et al., 2015; Faust et al., 2016; see Fig. 7) leading to decreased winter precipitation and overall arid conditions for this area.

5.2.4. The “wetter” Little Ice age

Slightly wetter conditions seem to have occured at LGA during the MCA-LIA transition. This is deduced by a slight decrease in the XRF PC1+, mostly triggered by an increase in the gypsum content [Ln(S/Ti) ratio] and the organic matter content [Ln(Br/Ti) ratio and TOC] (Fig. 6), which occurred at ~ 650 cal yr BP (~1300 CE) and until 350 cal yr BP (1600 CE). The end of the LIA is characterized by a significantly arid [detritic (PC1 +)] period between ~ 350–50 cal yr BP (1600–1900 CE), interrupted by a short relative humid event, inferred by an elevated TOC peak and gypsum-rich interval at around 200 cal yr BP (1750 CE). Even though NAO reconstructions show more negative phases during the LIA, implying higher winter precipitation in the Mediterranean region, paleoclimatic reconstructions from the area show a somehow wetter climate but drier than the previous IRHP (e.g., Martín-Puertas et al., 2010; Fig. 7).

5.2.5. The Industrial Era between 1850 CE and present

Arid conditions occurred at the beginning of the IE and between 1850 and 1957 CE, deduced by the positive values of XRF PC1 at LGA, suggesting more erosion and more detrital input (Figs. 6 and 7). This is confirmed by the low terrestrial and lake productivity [low C/N ratio, TOC and Ln(Br/Ti) ratio]. This agrees with other paleoclimatic reconstructions for that timespan, which show overall dry climate or ambiguous conditions (e.g., NAO reconstructions) (Fig. 7). For example, minima in precipitation estimations are inferred at that time from palynological studies in southern Iberia (Ilvonen et al., 2022).

5.2.5.1. Anthropogenic impact. The environmental inferences obtained from the interpretation of the sedimentary record shows that climate was the main forcing controlling environmental change, lake dynamics and sedimentation in LGA during the Late Holocene. However, an evident signal of human impact at LGA is the strong decrease in the C/N ratio and $\delta^{15}N$ and the increase in $\delta^{15}N$ and TOC values since 1944 CE (Fig. 3), suggesting eutrophication by algal blooms in the lake mostlikely due to the use of fertilizers in the nearby crops (Smith et al., 1999). Additionally, this abrupt decrease in $\delta^{15}N$ values mirrors a similar pattern registered in diverse North Hemisphere wetlands since the 1950 s, agreeing with the rise of reactive nitrogen emissions in the atmospheres as a consequence of the increasing fossil fuel consumption and the global development of the Haber-Bosch nitrogen fertilizer production (Holtgrieve et al., 2011). Finally, the period between 1965–2009 CE (−15 and −69 cal yr BP) in the LGA lake sediments was characterized by more productivity and enhanced grain size and sorting than earlier. This is interpreted by the minima in MS, XRF PC1, and maxima in TOC content, Ln(Br/Ti), Ln(S/Ti) and Ln(Zr/Rb) ratios, respectively. Gypsum occurred again abundantly since ~ 1993 CE until present (Figs. 4 and 7), which could have been related by a critical lake lowering and/or to enhanced organic matter input (notice the peak in TOC content; Fig. 3) that would have caused a lowering of the pH due to its oxidation effect favoring the precipitation of gypsum. Interestingly, the beginning of gypsum deposition at LGA also coincided with the beginning of intensive olive crop irrigation since the 90′s in the study area (Hidalgo Moya et al., 2007), requiring the spread of irrigation wells that produced a significant decrease in the piezometric levels of the aquifers (Hidalgo Moya et al., 2007). In addition, a synchronic decreasing trend in average precipitation has been recorded in the area. Perhaps the recent rapid increase in summer temperatures due to global warming (García-Alix et al., 2020), resulting in higher evapotranspiration and minimum lake levels, also generated an enhancement in the Ca^{2+}-SO_4^{2-} concentration in the lake waters further favoring gypsum precipitation. As a consequence, a reduction in lake levels by several meters has been recorded over the past few decades in LGA (Fig. 9D) and other Andalusian lakes. Water samplings conducted by the regional administration (Junta de Andalucía) after the lakes were declared a Natural Reserve in 1989 indicate a significant increase in water electrical conductivity in LGA and hypersaline conditions in the nearby LCA during this period (Fig. 9D). Further analysis suggests that LCA may have transitioned from a monomictic to a meromictic state because of the brine formation in the second half of 20th century (Rodríguez-Rodríguez et al., 2001).

The human-made damming structure observed in the LGA NW outflow area (see Fig. 9C) was most likely built in the last centuries and indicates the management and regulation of lake waters during phases of maximum lake levels. This dam had little impact on the lake sedimentation because it only functioned when the lake had a considerable height. This structure probably stopped being functional in recent decades (see last LGA lake phase in Fig. 9D discussed above) due to the considerable drop in the lake level, which no longer reaches the overflow.

6. Conclusions

The detailed sedimentological study of a sediment core from LGA in the southern Iberian Peninsula shows millennial- and centennial-scale variability during the past 3300 cal yr BP. Three periods, characterized by enhanced productivity and terrestrial vegetation input, increased sorting, as well as abundant gypsum precipitation, occurred between 3200–3100, 2600–1400, and −15 – −69 cal yr BP (1965–2009 CE). Gypsum precipitation during wetter climate stages (e.g. during the IRHP, 2600–1400 cal yr BP) was facilitated by increase in solutes supplied by the aquifer during times of high groundwater, mostly during warm/humid period as the IRHP (2600–1400 cal yr BP), or/and increased organic matter input.

Conversely, the periods characterized by main detritic sedimentation, with low productivity, low terrestrial organic matter input and lower reoxygenation of the lake waters, generally interpreted as arid, occurred (1) between ∼ 3050–2600 cal yr BP interrupted by short humid event ∼ 2830 cal yr BP; (2) between ∼ 1300–700 (650) cal yr BP and (3) between ∼ 350–50 cal yr BP, interrupted by a short relative humid interval at ∼ 200 cal yr BP. These climatic steps, such as the one that affected the area during the MCA (1300–650 cal yr BP), coincided in timing and duration with well-known arid events in the western Mediterranean. This suggests that sedimentary changes at LGA could have been triggered by millennial-scale climate variability, supporting a highly efficient climatic coupling between the North Atlantic and the western Mediterranean and alternation of persistent NAO + and NAO − modes as the main mechanism forcing millennial- and centennial-scale precipitation changes.

In addition, despite intense human activities have impacted the environments in the southern Iberian Peninsula over the past few millennia, climate appears to be the primary factor influencing sedimentation in the studied lake, instead of human-driven causes. Clear indications of human activity at LGA are a significant decrease in the C/N values and an increase in TOC content since 1944 CE, suggesting eutrophication caused by algae due to the use of fertilizers in nearby agricultural crops. This, together with the decreasing trend in precipitation, increase in maximum summer temperatures and increasing use of groundwater resources due to intensive irrigation of agricultural crops since the 1990 s, could have triggered the gypsum precipitation in the last few decades at LGA.

CRediT authorship contribution statement

Gonzalo Jiménez-Moreno: Writing – review & editing, Writing – original draft, Visualization, Supervision, Investigation, Funding acquisition, Formal analysis, Data curation, Conceptualization. **Antonio García-Alix:** Writing – review & editing, Project administration, Investigation, Funding acquisition, Formal analysis, Conceptualization. **Fernando Gázquez:** Writing – review & editing, Investigation. **Aurora Castillo-Baquera:** Investigation. **Lucía Martegani:** Visualization, Investigation. **Miguel Rodríguez-Rodríguez:** Writing – review & editing, Investigation. **Marta Rodrigo-Gámiz:** Writing – review & editing, Investigation, Funding acquisition. **Francisco J. Jiménez-Espejo:** Writing – review & editing, Investigation, Funding acquisition.

Declaration of competing interest

The authors declare that they have no known competing financial interests or personal relationships that could have appeared to influence the work reported in this paper.

Acknowledgements

This study was supported by projects PID2021-125619OB-C21/C22 and PID2021-123980OA-I00 (GYPCLIMATE), funded by the Ministerio de Ciencia e Innovación of Spain, the Agencia Estatal de Investigación and the Fondo Europeo de Desarrollo Regional FEDER MCIN/AEI/10.13039/501100011033/FEDER, UE” and CGL2017-85415-R,; Junta de Andalucía I + D + i Junta de Andalucía 2020 Retos P-20-00059, UGR-FEDER B-RNM-144-UGR18, UGR-FEDER A-RNM-336-UGR20, Project cofinanced by FEDER and LifeWatch-Eric LifeWatch-2019-10-UGR-01 and the research group RNM-190 (Junta de Andalucía). Funding also came from "Red de investigación temática PALEONET (RED24-153734-T) financiada por la Agencia Estatal de Investigación del Ministerio de Ciencia, Innovación y Universidades". F.G acknowledges the Ramón y Cajal fellowship, RYC2020-029811-I de la Agencia Estatal de Investigación and the grant PPIT-UAL, Junta de Andalucía-FEDER 2022-2026 (RyC-PPI2021-01). L.M. was funded by the FPU21/06924 grant of the Ministerio de Educación y Formación Profesional of Spain. We thank Raef Minwer-Barakat Requena and Alejandro López-Avilés who helped with the sediment sampling and the XRF scanning. We acknowledge Isabel Sánchez Almazo for the isotopic analysis at CIC-UGR. We are grateful to the keepers of the Natural Reserve of Lagunas de Archidona, and specially to África Lupión for support during field surveys and for providing historical monitoring data of the lake. We acknowledge three anonymous reviewers and the editor for making useful comments on a previous version of the manuscript.

Data availability

Geochemistry data LGA (Original data) (Google Drive)

References

Algeo, T.J., Liu, J., 2020. A re-assessment of elemental proxies for paleoredox analysis. Chemical Geology 540, 119549.

Amor, M., Busigny, V., Durand-Dubief, M., Tharaud, M., Ona-Nguema, G., Gélabert, A., Alphandéry, E., Menguy, N., Benedetti, M.F., Chebbi, I., Guyot, F., 2015. PNAS 112 (6), 1699–1703.

Anadón, P., Utrilla, R., Vázquez, A., 2000. Use of charophyte carbonates as proxy indicators of subtle hydrological and chemical changes in marl lakes: example from the Miocene Bicorb Basin, eastern Spain. Sedimentary Geology 133, 325–347.

Bahr, A., Jiménez-Espejo, F.J., Kolasinac, N., Grunert, P., Hernández-Molina, F.J., Röhl, U., Voelker, A.H.L., Escutia, C., Stow, D.A.V., Hodell, D., Alvarez-Zarikian, C. A., 2014. Deciphering bottom current velocityand paleoclimate signals from contourite deposits in the Gulf of Cadiz during the last 140 kyr: An inorganic geochemical approach. Geochem. Geophys. Geosyst., 15, 3145–3160.

Bellin, N., Vanacker, V., De Baets, S., 2013. Anthropogenic and climatic impact on Holocene sediment dynamics in SE Spain: A review. Quaternary International 308–309, 112–129.

Byrne, J., van der Laan, G., Figueroa, A., Qafoku, O., Wang, C., Pearce, C.I., Jackson, M., Feinberg, J., Rosso, K.M., Kappler, A., 2016. Size dependent microbial oxidation and reduction of magnetite nano- and micro-particles. Sci. Rep. 6, 30969.

Baker, A., et al., 2015. A composite annual-resolution stalagmite record of North Atlantic climate over the last three millennia. Sci. Rep. 5, 10307.

Bertrand, S., Tjallingii, R., Kylander, M.E., Wilheim, B., Roberts, S.J., Arnaud, F., Brown, E., Bindler, R., 2024. Inorganic geochemistry of lake sediments: A review of analytical techniques and guidelines for data interpretation. Eart-Science Reviews 249, 104639.

Blaauw, M., Christen, J.A., 2011. Flexible paleoclimate age-depth models using an autoregressive gamma process. Bayesian Anal. 6, 457–474.

Brenner, M., Whitmore, T., Curtis, J., Hodell, D., Schelske, C., 1999. Stable isotope ($\delta^{13}C$ and $\delta^{15}N$) signatures of sedimented organic matter as indicators of historic lake trophic state. Journal of Paleolimnology 22, 205–221.
Calaforra, J.M., Pulido-Bosch, A., 1999. Gypsum karst features as evidence of diapiric processes in the Betic Cordillera. Southern Spain. Geomorphology 29 (3–4), 251–264.
Camuera, J., Jiménez-Espejo, F.J., Soto-Chica, J., Jiménez-Moreno, G., García-Alix, A., Ramos-Román, M.J., Ruha, L., Castro-Prieto, M., 2023. Drought as a possible contributor to the Visigothic Kingdom crisis and Islamic expansion in the Iberian Peninsula. Nature Communications 14, 5733.
Caracterización Ambiental de Humedales en Andalucía, 2005. Consejería de Medio Ambiente. Junta de Andalucía. 511 pp.
Carrasco, F., Andreo, B., Liñán, C., Mudary, M., 2004. The gypsum karst of the Los Hoyos area (Malaga, southern Spain): A geomorphological and hydrogeological study. In "Karst and Tectonics" (pp. 189-208). Geological Society, London, Special Publications.
Carrión, J.S., 2002. Patterns and processes of Late Quaternary environmental change in a montane region of southwestern Europe. Quaternary Science Reviews 21, 2047–2066.
Choudhury, M.I., Urrutia-Cordero, P., Zhang, H., Ekvall, M.K., Medeiros, L.R., Hansson, L.-A., 2019. Charophytes collapse beyond a critical warming and brownification threshold in shallow lake systems. Science of the Total Environment 661, 148–154.
Chung, F.H., 1975. Quantitative interpretation of X-ray diffraction patterns of mixtures. III. Simultaneous determination of a set of reference intensities. Journal of Applied Crystallography 8, 17–19.
Cohen, A.S., 2003. Paleolimnology: The History and Evolution of Lake Systems. Oxford University Press.
Combourieu Nebout, N., Peyron, O., Dormoy, I., Desprat, S., Beaudouin, C., Kotthoff, U., Marret, F., 2009. Rapid climatic variability in the west Mediterranean during the last 25000 years from high resolution pollen data. Climate of the past 5, 503–521.
Dypvik, H., Harris, N.B., 2001. Geochemical facies analysis of fine-grained siliciclastics using Th/U, Zr/Rb and (Zr+Rb)/Sr ratios. Chemical Geology 181, 131–146.
Enders, S.K., Pagani, M., Pantoja, S., Baron, J.S., Wolfe, A.P., Pedentchouk, N., Nuñez, L., 2008. Compound-specific stable isotopes of organic compounds from lake sediments track recent environmental changes in an alpine ecosystem, Rocky Mountain National Park. Colorado. Limnology and Oceanography 53. https://doi.org/10.4319/lo.2008.53.4.1468.
Evans, N.P., Bauska, T.K., Gázquez, F., Brenner, M., Curtis, J.H., Hodell, D.A., 2018. Quantification of drought during the collapse of the classic Maya civilization. Science 361 (6401), 498–501.
Faust, J.C., Fabian, K., Milzer, G., Giraudeau, J., Knies, J., 2016. Norwegian fjord sediments reveal NAO related winter temperature and precipitation changes of the past 2800 years. Earth and Planetary Science Letters 435, 84–93.
Fletcher, W., Boski, T., Moura, D., 2007. Palynological evidence for environmental and climatic change in the lower Guadiana valley (Portugal) during the last 13,000 years. The Holocene 17, 479–492.
Galimov, E.M., 1985. The biological fractionation of isotopes. Academic Press, Orlando.
Gázquez, F., Bauska, T.K., Comas-Bru, L., Ghaleb, B., Calaforra, J.-M., Hodell, D.A., 2020. The potential of gypsum speleothems for paleoclimatology: Application to the Iberian Roman Humid Period. Sci. Rep. 10, 14705.
Gil-Márquez, J.M., Mudarra, M., Andreo, B., Linares, L., Carrasco, F., Benavente, J., 2016. Hydrogeological characterization of the Salinas-Los Hoyos evaporitic karst (Malaga province, S Spain) using topographic, hydrodynamic, hydrochemical and isotopic methods. 2016. Acta Carsologica 45/1, 147-160.
Gázquez, F., Jiménez-Espejo, F.J., Rodríguez-Rodríguez, M., Martegani, L., Voigt, C., Ruíz-Lara, D., Moreno, A., Valero-Garcés, B., Morellón, M., Martín-Puertas, C., 2023. Roman water management impacted the hydrological functioning of wetlands during drought periods. Sci. Rep. 13, 18815.
Guevara, S.R., Rizzo, A., Daga, R., Williams, N., Villa, S., 2019. Bromine as indicator of source of lacustrine sedimentary organic matter in paleolimnological studies. Quaternary Research 92, 257–271.
Hammer, Ø., Harper, D.A.T., Ryan, P.D., 2001. PAST: Paleontological statistics software package for education and data analysis. Palaeontologia Electronica 4 (1), 9.
Hasan, A.S.M.M., Hossain, I., Rahman, M.A., Zaman, M.N., Biswas, P.K., Alam, M.S., 2022. Chemistry and mineralogy of Zr- and Ti-rich minerals sourced from Cox's Bazar beach placer deposits, Bangladesh: Implication of resources processing and evaluation. Ore Geology Reviews 141, 104687.
Hervás-Gámez, C., Delgado-Ramos, F., 2019. Drought Management Planning Policy: From Europe to Spain. Sustainability 11 (6), 1862.
Hidalgo Moya, J., Vega Macías, V., Hidalgo Moya, J.C., 2007. Riego del olivar en Andalucía. Agricultura 896, 376–382.
Hodell, D.A., Anselmetti, F.S., Ariztegui, D., Brenner, M., Curtis, J.H., Gilli, A., Grzesik, D.A., Guilderson, T.J., Muller, A.D., Bush, M.B., Correa-Metrio, Y.A., Escobar, J., Kutterolf, S., 2008. An 85-ka record of climate change in lowland Central America. Quat. Sci. Rev. 27, 1152–1165.
Holtgrieve, G.W., Schindler, D.E., Hobbs, W.O., Leavitt, P.R., Ward, E.J., Bunting, L., Chen, G., Finney, B.P., Gregory-Eaves, I., Holmgren, S., Lisac, M.J., Lisi, P.J., Nydick, K., Rogers, L.A., Saros, J.E., Selbie, D.T., Shapley, M.D., Walsh, P.B., Wolfe, A.P., 2011. A coherent signature of anthropogenic nitrogen deposition to remote watersheds of the Northern Hemisphere. Science 334, 1545–1548.
Hubbard, C.R., Snyder, R.L., 1988. Reference Intensity Ratio - Measurement and Use in Quantitative XRD. Powder Diffr. 3, 74–78.
Hurrell, J.W., Kushnir, Y., Ottersen, G., Visbeck, M., 2013. An Overview of the North Atlantic Oscillation. In: The North Atlantic Oscillation: Climatic Significance and Environmental Impact. American Geophysical Union, pp. 1–35.
Ilvonen, L., López-Sáez, J.A., Holmström, L., Alba-Sánchez, F., Pérez-Díaz, S., Carrión, J. S., Ramos-Román, M.J., Camuera, J., Jiménez-Moreno, G., Ruha, L., Seppä, H., 2022. Spatial and temporal patterns of Holocene precipitation change in the Iberian Peninsula. Boreas 51, 776–792.
IPCC, 2022. Climate Change 2022: Impacts, Adaptation, and Vulnerability. Contribution of Working Group II to the Sixth Assessment Report of the Intergovernmental Panel on Climate Change [H.-O. Pörtner, D.C. Roberts, M. Tignor, E.S. Poloczanska, K. Mintenbeck, A. Alegría, M. Craig, S. Langsdorf, S. Löschke, V. Möller, A. Okem, B. Rama (eds.)]. Cambridge University Press. Cambridge University Press, Cambridge, UK and New York, NY, USA, 3056 pp.
Jiménez-Bonilla, A., Rodríguez-Rodríguez, M., Yanes, J.L., Gázquez, F., 2023. Hydrological modelling and evolution of lakes and playa-lakes in southern Spain constrained by geology, human management and climate change. Science of the Total Environment 905, 167183.
Jiménez-Espejo, F.J., Garcia-Alix, A., Jiménez-Moreno, G., Martínez-Ruiz, F., Anderson, R.S., Rodríguez-Tovar, F.J., Giralt, S., Rodrigo-Gámiz, M., Delgado-Huertas, A., Pardo-Igúzquiza, E., 2014. Climate change and Saharan Aeolian input variations over western Europe during the Holocene. Chemical Geology 374–375, 1–12.
Jiménez-Moreno, G., García-Alix, A., Hernández-Corbalán, M.D., Anderson, R.S., Delgado-Huertas, A., 2013. Vegetation, fire, climate and human disturbance history in the southwestern Mediterranean area during the late Holocene. Quat. Res. 79, 110–122.
Jiménez-Moreno, G., Rodríguez-Ramírez, A., Pérez-Asensio, J.N., Carrión, J.S., López-Sáez, J.A., Villarías-Robles, J.J., Celestino-Pérez, S., Cerrillo-Cuenca, E., León, A., 2015. Impact of late-Holocene aridification trend, climate variability and geodynamic control on the environment from a coastal area in SW Spain. Holocene 25, 607–617.
Jiménez-Moreno, G., García-Alix, A., Anderson, R.S., Ramos-Román, M.J., Camuera, J., Mesa-Fernández, J.M., Toney, J.L., Jiménez-Espejo, F.J., Carrión, J.S., López-Avilés, A., Rodrigo-Gámiz, M., Webster, C.E., 2022. Reconstruction of past environment and climate using wetland sediment records from the Sierra Nevada. In: R. Zamora and M. Oliva (eds.), The Landscape of the Sierra Nevada, Springer Nature Switzerland AG, 95-114.
Ketterer, M.E., Hafer, K.M., Jones, V.J., Appleby, P.G., 2004. Rapid Dating of Recent Sediments in Loch Ness: Inductively Coupled Plasma Mass Spectrometric Measurements of Global Fallout Plutonium. The Science of the Total Environment 322, 221–229.
Kylander, M.E., Ampel, L., Wohlfarth, B., Veres, D., 2011. High-resolution X-ray fluorescence core scanning analysis of Les Echets (France) sedimentary sequence: new insights from chemical proxies. Journal of Quaternary Science 26 (1), 109–117.
Leri, A.C., Myneni, S.C.B., 2012. Natural organobromine in terrestrial ecosystems. Geochimica et Cosmochimica Acta 77, 1–10.
López-Avilés, A., Jiménez-Moreno, G., García-Alix, A., García-García, F., Camuera, J., Anderson, R.S., Sanjurjo-Sánchez, J., Chamorro, C.A., Carrión, J.S., 2022. Post-glacial evolution of alpine environments in the western Mediterranean region: The Laguna Seca record. Catena 211, 106033.
Magny, M., 2004. Holocene climate variability as reflected by mid-European lake-level fluctuations and its probable impact on prehistoric human settlements. Quaternary International 113, 65–79.
Makri, S., Wienhues, G., Bigalke, M., Gilli, A., Rey, F., Tinner, W., Vogel, H., Grosjean, M., 2021. Variations of sedimentary Fe and Mn fractions under changing lake mixing regimes, oxygenation and land surface processes during Late-glacial and Holocene times. Science of the Total Environment 755, 143418.
Margaritelli, G., Cacho, I., Català, A., Barra, M., Bellucci, L.G., Lubritto, C., Rettori, R., Lirer, F., 2020. Persistent warm Mediterranean surface waters during the Roman period. Scientific Reports 10, 10431.
Martín-Puertas, C., Valero-Garcés, B.L., Mata, M.P., González-Sampériz, P., Bao, R., Moreno, A., Stefanova, V., 2008. Arid and humid phases in southern Spain during the last 4000 years: the Zonar Lake record, Cordoba. The Holocene 18, 907–921.
Martín-Puertas, C., Valero-Garcés, B.L., Brauer, A., Mata, M.P., Delgado-Huertas, A., Dulski, P., 2009. The Iberian–Roman Humid Period (2600–1600 cal yr BP) in the Zoñar Lake varve record (Andalucía, southern Spain). Quat. Res. 71, 108–120.
Martín-Puertas, C., Jiménez-Espejo, F., Martínez-Ruiz, F., Nieto-Moreno, V., Rodrigo, M., Mata, M.P., Valero-Garcés, B.L., 2010. Late Holocene climate variability in the southwestern Mediterranean region: an integrated marine and terrestrial geochemical approach. Clim. past 6, 807–816.
McLauchlan, K., Williams, J., Craine, J., Jeffers, E., 2013. Changes in global nitrogen cycling during the Holocene epoch. Nature 495, 352–355.
MedECC, 2020. Climate and Environmental Change in the Mediterranean Basin – Current Situation and Risks for the Future. First Mediterranean Assessment Report [Cramer, W., Guiot, J., Marini, K. (eds.)] Union for the Mediterranean, Plan Bleu, UNEP/MAP, Marseille, France, 632pp.
Mediavilla, R., Santisteban, J.I., López-Cilla, I., Galán de Frutos, L., de la Hera-Portillo, A., 2020. Climate-Dependent Groundwater Discharge on Semi-Arid Inland Ephemeral Wetlands: Lessons from Holocene Sediments of Lagunas Reales in Central Spain. Water 12, 1911.
Mesa-Fernández, J.M., Jiménez-Moreno, G., Rodrigo-Gámiz, M., García-Alix, A., Jiménez-Espejo, F.J., Martínez-Ruiz, F., Anderson, R.S., Camuera, J., Ramos-Román, M.J., 2018. Vegetation and geochemical responses to Holocene rapid climate change in the Sierra Nevada (southeastern Iberia): the Laguna Hondera record. Climate of the past 14, 1687–1706.
Meyers, P.A., 1994. Preservation of elemental and isotopic source identification of sedimentary organic matter. Chemical Geology 113, 289–302.

Meyers, P.A., 2003. Applications of organic geochemistry to paleolimnological reconstructions: a summary of examples from the Laurentian Great Lakes. Org. Geochem. 34, 261–289.
Meyers, P.A., Teranes, J.L., 2001. Sediment organic matter. In: Last, W.M., Smol, J.P. (Eds.), Tracking Environmental Changes Using Lake Sediments, vol. 2. Kluwer Academic Publishers, Dordrecht, pp. 239–270.
Moreno, A., Pérez, A., Frigola, J., Nieto-Moreno, V., Rodrigo-Gámiz, M., Martrat, B., González-Sampériz, P., Morellón, M., Martín-Puertas, C., Corella, J.P., Belmonte, Á., Sancho, C., Cacho, I., Herrera, G., Canals, M., Grimalt, J.O., Jiménez-Espejo, F., Martínez-Ruiz, F., Vegas-Vilarrúbia, T., Valero-Garcés, B.L., 2012. The Medieval Climate Anomaly in the Iberian Peninsula reconstructed from marine and lake records, Quaternary Sci. Rev., 43, 16–32.
Naeher, S., Gilli, A., North, R.P., Hamann, Y., Schubert, C.J., 2013. Tracing bottom water oxygenation with sedimentary Mn/Fe ratios in Lake Zurich. Switzerland. Chem. Geol. 352, 125–133.
Nieto-Moreno, V., Martínez-Ruiz, F., Giralt, S., Jiménez-Espejo, F., Gallego-Torres, D., Rodrigo-Gámiz, M., García-Orellana, J., Ortega-Huertas, M., de Lange, G.J., 2011. Climate of the past Discussion 7, 635–675.
O'Leary, M.H., 1981. Carbon isotope fractionation in plants. Phytochemistry 20, 553–567.
O'Leary, M.H., 1988. Carbon isotopes in photosynthesis. Bioscience 38, 328–336.
Olivares-Casillas, G., Correa-Metrio, A., Zawisza, E., Wojewódka-Przybył, M., Blaauw, M., Romero, F., 2021. Environmental variability during the last three millennia in the rain shadows of central Mexico. Boletín De La Sociedad Geológica Mexicana 73 (1), A171220.
Olsen, J., Anderson, N.J., Knudsen, M.F., 2012. Variability of the North Atlantic Oscillation over the past 5,200 years. Nat. Geosci., 5, 808–812.
PAGES2k Consortium., 2017. A global multiproxy database for temperature reconstructions of the Common Era. Scientific Data 4, 170088.
Parsons, D.F., Hayashi, M., van der Kamp, G., 2002. Infiltration and solute transport under a seasonal wetland: Bromide tracer experiments in Saskatoon. Canada. Hydrol. Process. 18, 2011–2027.
Páscoa, P., Gouveia, C.M., Russo, A., Trigo, R.M., 2017. Drought trends in the Iberian Peninsula over the last 112 years. Adv. Meteorol. 2017, 4653126.
Peña-Gallardo, M., Vicente-Serrano, S.M., Domínguez-Castro, F., et al., 2019. Assessing impacts of climate variability and extremes on food security: the case of drought in Spain. Agricultural Systems 163, 113–125.
Ramos-Román, M.J., Jiménez-Moreno, G., Anderson, R.S., García-Alix, A., Toney, J.L., Jiménez-Espejo, F.J., Carrión, J.S., 2016. Centennial-scale vegetation and North Atlantic Oscillation changes during the Late Holocene in the southern Iberia. Quaternary Science Reviews 143, 84–95.
Ramos-Román, M.J., Jiménez-Moreno, G., Camuera, J., García-Alix, A., Anderson, R.S., Jiménez-Espejo, F.J., Carrión, J.S., 2018. Holocene climate aridification trend and human impact interrupted by millennial- and centennial-scale climate fluctuations from a new sedimentary record from Padul (Sierra Nevada, southern Iberian Peninsula). Climate of the past 14, 117–137.
Reed, J.M., Stevenson, A.C., Juggins, S., 2001. A multi-proxy record of Holocene climatic change in southwestern Spain: the Laguna de Medina, Cádiz. The Holocene 11, 707–719.
Reimer, P.J., Austin, W.E.N., Bard, E., Bayliss, A., Blackwell, P.G., Bronk Ramsey, C., Butzin, M., Cheng, H., Edwards, R.L., Friedrich, M., Grootes, P.M., Guilderson, T.P., Hajdas, I., Heaton, T.J., Hogg, A.G., Hughen, K.A., Kromer, B., Manning, S.W., Muscheler, R., Palmer, J.G., Pearson, C., van der Plicht, J., Reimer, R.W., Richards, D.A., Scott, E.M., Southon, J.R., Turney, C.S.M., Wacker, L., Adolphi, F., Büntgen, U., Capano, M., Fahrni, S.M., Fogtmann-Schulz, A., Friedrich, R., Kohler, P., Kudsk, S., Miyake, F., Olsen, J., Reinig, F., Sakamoto, M., Sookdeo, A., Talamo, S., 2020. The IntCal20 Northern Hemisphere Radiocarbon Age Calibration Curve (0–55 cal kBP). Radiocarbon 62, 725–757.
Rivas-Martínez, S., 1987. Memoria del mapa de series de vegetación de España. Ministerio de Agricultura, Pesca y Alimentación, Madrid.
Rodrigo-Gámiz, M., Martínez-Ruíz, F., Jiménez-Espejo, F.J., Gallego-Torres, D., Nieto-Moreno, V., Romero, O., Ariztegui, D., 2011. Impact of climate variability in the western Mediterranean during the last 20,000 years: Oceanic and atmospheric responses. Quat. Sci. Rev. 30, 2018–2034.
Rodríguez-Rodríguez, M., 2002. Contribución hidrogeológica y limnológica a la caracterización ambiental de zonas húmedas de Andalucía Oriental. University of Granada. PhD dissertation.
Rodríguez-Rodríguez, M., Benavente, J., 2008. Definition of wetland typology for hydro-morphological elements within the WFD: A case study from southern Spain. Water Resources Management 22 (7), 797–821.
Rodríguez-Rodríguez, M., Cruz Pizarro, L., Cruz Sanjulián, J.J., Benavente, J., Almécija, C., 2001. Caracterización limnológica de dos lagunas saladas del sur de la Península Ibérica. Limnetica 20 (2), 233–243.
Smith, V.H., Tilman, G.D., Nekola, J.C., 1999. Eutrophication: Impacts of excess nutrient inputs on freshwater, marine, and terrestrial ecosystems. Environmental Pollution 100 (1–3), 179–196.
Snowball, I., Sandgren, P., 2001. Application of mineral magnetic techniques to paleolimnology. In: Last, W.M., Smol, J.P. (Eds.), Tracking Environmental Changes Using Lake Sediments, vol. 2. Kluwer Academic Publishers, Dordrecht, pp. 217–237.
Sousa, P.M., Barriopedro, D., Ramos, A.M., García-Herrera, R., Espírito-Santo, F., Trigo, R.M., 2019. Saharan air intrusions as a relevant mechanism for Iberian heatwaves: the record breaking events of August 2018 and June 2019. Weather Clim. Extr. 26, 100224.
Talbot, M.R., Laerdal, T., 2000. The Lake Pleistocene-Holocene palaeolimnology of Lake Victoria, East Africa, based upon elemental and isotopic analyses of sedimentary organic matter. J. Paleolimnol. 23, 141–164.
Teranes, J.L., Bernasconi, S.M., 2000. The record of nitrate utilization and productivity limitation provided by δ^{15}N values in lake organic matter—a study of sediment trap and core sediments from Baldeggersee. Switzerland. Limnol. Oceanogr. 45, 801–813.
Trouet, V., Esper, J., Graham, N.E., Baker, A., Scourse, J.D., Frank, D.C., 2009. Persistent Positive North Atlantic Oscillation Mode Dominated the Medieval Climate Anomaly. Science 324, 78–80.
Vegas-Vilarrúbia, T., Corella, J.P., Pérez-Zanón, N., Buchaca, T., Trapote, M.C., López, P., Sigró, J., Rull, V., 2018. Historical shifts in oxygenation regime as recorded in the laminated sediments of lake Montcortès (Central Pyrenees) support hypoxia as a continental-scale phenomenon. Science of the Total Environment 612, 1577–1592.
Vera, J.A., 2004. Evolution of the Iberian Continental Margin. In: Geology of Spain. Geological Society of London, pp. 394–409.
Vizcaino, A., Jiménez-Espejo, F.J., Dunbar, R.B., Mucciarone, D., García-Alix, A., Neugebauer, I., Ariztegui, D., 2022. Southern Hemisphere Westerly Winds have modulated the formation of laminations in sediments of Lago Fagnano (Tierra del Fuego, Argentina) over the past 6.3 ka. Boreas 52, 124–138.
Weltje, G.J., Tjallingii, R., 2008. Calibration of XRF core scanners for quantitative geochemical logging of sediment cores: Theory and application. Earth and Planetary Science Letters 274, 423–438.
Wu, L., Wilson, D.J., Wang, R., Yin, X., Chen, Z., Xiao, W., Huang, M., 2020. Evaluating Zr/Rb ratio from XRF scanning as an indicator of grain-size variations of glaciomarine sediments in the Southern Ocean. Geochem. Geophys. Geosyst., 21, e2020GC009350.
Zazo, C., Mercier, N., Silva, P.G., Dabrio, C.J., Goy, J.L., Lario, J., Roquero, E., Bardají, T., Ghaleb, B., Cabero, A., Soler, V., 2005. Landscape evolution and geodynamic controls in the Gulf of Cadiz (Huelva coast, SW Spain) during the Late Quaternary. Geomorphology 68, 269–290.